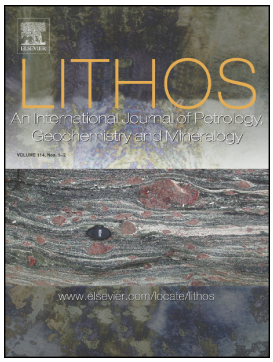

The Andaluca plutonic unit, Vinquis Intrusive Complex, Argentina: An assessment of mantle role in the genesis of Early Carboniferous weakly peraluminous A-type granites in the pre-Andean SW Gondwana margin

Matías M. Morales Cámera, Juan A. Dahlquist, Juan A. Moreno, Priscila S. Zandomeni, Marcos Garcia-Arias, Miguel A.S. Basei

PII: S0024-4937(22)00282-1

DOI: https://doi.org/10.1016/j.lithos.2022.106873

Reference: LITHOS 106873

To appear in: *LITHOS*

Received date: 20 December 2021

Revised date: 18 August 2022

Accepted date: 6 September 2022

Please cite this article as: M.M. Morales Cámera, J.A. Dahlquist, J.A. Moreno, et al., The Andaluca plutonic unit, Vinquis Intrusive Complex, Argentina: An assessment of mantle role in the genesis of Early Carboniferous weakly peraluminous A-type granites in the pre- Andean SW Gondwana margin, *LITHOS* (2022), https://doi.org/10.1016/j.lithos.2022.106873

The Andaluca plutonic unit, Vinquis Intrusive Complex, Argentina: an assessment of mantle role in the genesis of Early Carboniferous weakly peraluminous A-type granites in the pre- Andean SW Gondwana margin

Matías M. Morales Cámera[a,b,*], *Juan A. Dahlquist* [a,b], *Juan A. Moreno*[c], *Priscila S. Zandomeni* [a,b], *Marcos Garcia-Arias*[d], *Miguel A.S. Basei*[e]

[a] Universidad Nacional de Córdoba. Facultad de Ciencias Exactas, Físicas y Naturales, Av. Vélez Sarsfield 1611, Córdoba, Argentina.

[b] Consejo Nacional de Investigaciones Científicas y Tecnológicas (CONICET), Centro de investigaciones en Ciencias de la Tierra, (CICTERRA), Av. Vélez Sarsfield 1611, Córdoba, Argentina.

[c] Departamento de Mineralogía y Petrología, Universidad Complutense (UCM), 28040 Madrid, Spain.

[d] Departamento de Geología, Universidad de Salamanca (USAL), 37008 Salamanca, Spain.

[e] Instituto de Geociências da Universidade de São Paulo, Rua do Lago 562, 05508-080, São Paulo, SP, Brasil.

* Corresponding author.

E-mail address: matiasmmoralesc@unc.edu.ar (M.M. Morales Cámera). *Telephone number: +54-9-351-3464598*

Abstract

During the Early Carboniferous, significant intracontinental magmatism was developed in the retro-arc region of the SW margin of Gondwana between ca. 27° and 31°S. This magmatism consisted of metaluminous to weakly peraluminous A-type granites, strongly peraluminous A-type granites (A- to S- hybrid granitoids) and, in a lesser extent, (sub-)volcanic felsic (rhyolites and trachytes) and mafic (alkaline basalts and lamprophyres) rocks. The Vinquis Intrusive Complex (VIC) registers these two compositional varieties of A-type granites: the Vinquis Unit (VU) represents the strongly peraluminous granites and the Andaluca Unit (AU) the weakly peraluminous granites. The adjacent Zapata Intrusive Complex (ZIC) also contains metaluminous to weakly peraluminous A-type granites. The AU is a semi-elliptical plutonic body of approximately 60 km^2 located in the southwestern part of the VIC, intruding the Vinquis Unit. The AU comprises three dominant rock types: i) quartz monzonite, ii) syenogranite and iii) alkali feldspar granite that can be classified as F-rich (calculated F content: 1950-5700 ppm), ferroan ($FeO^t/(FeO^t+MgO)$= 0.86-0.95) and weakly peraluminous (ASI= 1.03-1.10) A-type (Zr+Nb+Ce+Y= 364-570 ppm; Ga=20-23 ppm) granitoids (SiO_2 wt.% = 67.8-75.4% wt.%). This unit was emplaced in early Carboniferous time (U-Pb zircon crystallization ages of 346 ± 3 Ma and 342 ± 3 Ma). The AU has $^{87}Sr/^{86}Sr_t$, εNd_t and εHf_t values ranging from 0.7092 to 0.7140, −7.6 to −3.6 and −16.5 to −3.3, respectively. These isotopic suggest that the parental magma of AU dominantly involved variable mixtures of mantle-derived components (magmas/fluids) and peraluminous continental crust. The extremely felsic granites of the AU (SiO_2 > ~72%) with a strongly fractionated composition (Rb > 336 and Sr < 70 ppm and Eu/Eu* < 0.22) supports extensive fractional crystallization. The high contents of fluorine and HFSE in AU could be explained as derived from an F- HFSE- and alkali-rich parental mafic magma plus contributions from F-bearing minerals assimilated from the country rock. Likewise, the magmatic differentiation processes from these reduced mafic magmas could explain the ferroan character of the AU granitoids. We envision three stages in the origin of these rocks: (1) fluids and magmas from the asthenospheric mantle metasomatize and melt the subcontinental lithospheric mantle (SCLM), the alkali-rich mafic melts produced are emplaced at the base of the crust, transfer heat to the crust and melt it generating strongly peraluminous A-type magmas; (2) continued introduction of alkali-rich mafic magmas into the deep crust produce extensive assimilation of the preheated crust in equilibrium with mafic cumulates (generated by reaction and/or fractionation); (3) the hot magmas so produced migrate into the middle-upper crust to produce ferroan weakly peraluminous A-type granitoids.

Keywords: Ferroan granites, Fluorine-rich granitic magma, intracontinental magmatism, Igneous Geochemistry, U-Pb dating, Hf and Nd isotopes

1. Introduction

A-type granites form a major igneous rock type that encompasses a large and diverse number of granitoids (Dall'Agnol et al., 2012) which nevertheless have some characteristics in common. These granites are usually present in anorogenic to post-orogenic or intracontinental settings. They have generally high SiO_2, alkalis, halogens (F and Cl) and HFSE (REE, Zr, Nb, Y) contents, high Fe/Mg and Ga/Al ratios, and low contents of trace elements compatible in mafic minerals (Co, Cr. Ni) and feldspars (Ba, Sr) (Bonin, 2007; Dahlquist et al., 2010; Eby, 1990; Whalen et al., 1987). Although initially described as peralkaline (Loselle and Wones, 1979), metaluminous and peraluminous varieties have been later included (Collins et al., 1982; Eby, 1990).

The main petrogenetic processes proposed to generate A-type granites are diverse: (1) differentiation of mantle-derived basaltic magmas (± crust assimilation) (Loiselle and Wones, 1979; Frost and Frost, 2011), (2) partial melting of quartzofeldspathic crustal rocks (Creaser et al., 1991; Skjerlie and Johnston, 1992; Patiño Douce, 1997), (3) partial melting of a lower crustal source from which melt was extracted previously (Collins et al., 1982), and (4) melting of a crust metasomatized by percolation of alkali fluids derived from a degassing mantle (Martin, 2006; Moreno et al., 2016). This wide compositional spectrum of rocks and processes, occasionally confusing or ambiguous (Bonin, 2007; Frost and Frost, 2011), becomes even more complex when rocks with hybrid or transitional characteristics such as A + I granitoids (e.g., Wang et al., 2021) and A + S granitoids (e.g., Morales Cámera et al., 2017, 2020) appear.

In this sense, the extensive Devonian foreland and Carboniferous retro-arc magmatism developed in the SW margin of Gondwana, present in the Eastern Sierras Pampeanas of Argentina (Fig. 1), is an excellent example to assess the compositional variability and petrogenesis of A-type magmas. Three major varieties of granitoids have been recognized in the referred region: i) metaluminous to weakly peraluminous A-type granites, ii) strongly peraluminous A-type granites (A- to S- hybrid granitoids) and iii) metaluminous I- to A-type hybrid granitoid suites (Dahlquist et al., 2021; López de Luchi et al., 2017).

The Sierra de Vinquis, a mountain range (560 km^2) in the Eastern Sierras Pampeanas, registers part of the aforementioned Devonian-Carboniferous magmatism (Fig. 1). Until a few years ago, the geology of this mountainous block was poorly known, with only a few works published about the topic (González Bonorino, 1972; Sosic, 1972; Toselli et al., 1992), but nevertheless it was generally considered in the regional context to be made up of granitoids formed during the Ordovician Famatinian orogeny (e.g., Dahlquist et al., 2013; Grosse et al., 2011). Recently, Morales Cámera et al. (2017), based on new mineral and whole-rock chemistry, geochronological and isotopic data, established that the eastern flank of the Sierra de Vinquis, named here as the Vinquis Unit (VU), is composed of F-rich strongly peraluminous A-type granites emplaced in the latest Devonian or earliest Carboniferous time (355 ± 7 Ma, U-Pb

zircon dating) (Fig. 1). In the western flank of the Sierra de Vinquis, a subcircular plutonic body (named here as the Andaluca Unit, AU), formed by weakly peraluminous ferroan biotitic granitoids (A-type) intruding the VU, was preliminarily identified (Morales Cámera, 2019). Thus, based on previous and new data, the Sierra de Vinquis is made up of two main intrusive units, (1) the older Vinquis Unit and (2) the younger Andaluca Unit, which together form the Vinquis Intrusive Complex (VIC) (Fig. 2).

In this work, we present extensive field geology, detailed petrography and whole-rock chemistry data including major and trace elements, mineral compositions and whole-rock Rb-Sr and Sm-Nd isotope data for the Andaluca Unit, plus some complementary data for the Vinquis Unit and the adjacent Carboniferous Zapata Intrusive Complex (Fig. 2). In addition, three new sets of in situ U-Pb zircon ages and Hf isotopic data for the Vinquis Intrusive Complex are also reported. From this data set we seek to assess the magma sources and the petrogenetic processes that led to the parental magma composition and the subsequent evolution of the Andaluca Unit, with implications for the tectonic evolution of the Early Carboniferous magmatism in the Eastern Sierras Pampeanas and the controversial origin of the A-type granites. Finally, we investigate the role of fluids in the petrogenesis of the AU through the estimation of its F and Cl contents.

2. Geological Setting for the Devonian - Carboniferous magmatism

The proto-Andean margin of Gondwana was a long-lived active margin (Cawood, 2005; Nelson and Cottle, 2018) starting in the Early Paleozoic (e.g., Casquet et al., 2018; Rapela et al., 2018), a situation that has continued intermittently to the present. It underwent a number of magmatic episodes and hypothetical collisions of microcontinents. Part of this history is preserved in the Sierras Pampeanas and the Cordillera Frontal of NW Argentina (Fig. 1), now exposed due to Andean tilting and compression since the Miocene related to the flattening of the subduction angle of the Nazca plate (e.g., Jordan and Allmendinger, 1986; Mardonez et al., 2020; Ramos et al., 2002). Geochronological data show four main Palaeozoic magmatic events mostly represented in the Sierras Pampeanas and the Cordillera Frontal (Fig. 1): 1) *Pampean magmatism*, 515-535 Ma, 2) *Famatinian magmatism*, 463-484 Ma, 3) *Devonian magmatism*, 366-413 Ma and 4) *Carboniferous magmatism*, 322-357 Ma (e. g., Casquet et al., 2018; Dahlquist et al., 2021; Rapela et al., 2018; and reference therein).

Regarding the Devonian and Carboniferous magmatism, a review by Dahlquist et al. (2021) in the Sierras Pampeanas and Frontal Cordillera between 27° and 35°S distinguished four main magmatic domains: 1) Devonian Arc, 2) Devonian Foreland, 3) Carboniferous Arc, and 4) Carboniferous Retro-Arc. According to these authors, the type of magmatism in each domain was controlled by changes in the subduction configuration on a long-lived active convergent margin.

The Devonian magmatism would have been the result of a segmented subduction, with the development of a calc-alkaline arc between 34° and 35°S and with a horizontal subduction and no arc between 27° and 33°S. Within the arc-absent setting, at 31º-33º30'S, an extended granitic magmatism in the

foreland with a distinctive presence of small-scale high silica adakites was developed above a resubduction zone at least 800 km away from the continental margin. The main exponent of this intracontinental magmatism is the Achala batholith (Fig. 1), which is mainly composed of F-rich moderately to strongly peraluminous A-type granites (Dahlquist et al., 2013, 2014; Morales Cámera et al., 2020).

During the latest Devonian to Carboniferous, a roll-back process led to 'normal' ocean slab subduction, to an extensional regime and to increased convective mantle upwelling in the intracontinental region between 27° and 31°S (Alasino et al., 2012; Dahlquist et al., 2021 and references therein). Coetaneous arc and retro-arc magmatism displaying a northward migration were developed. The arc plutons, located in Western Sierras Pampeanas and Cordillera Frontal, have a calc-alkaline signature (Alasino et al., 2012; Moreno et al., 2020 and references therein). The retro-arc magmatism, currently located in the Eastern Sierras Pampeanas, has a granitic A-type (metaluminous and peraluminous) geochemical signature with participation of both mantle material (lithospheric and/or asthenospheric mantle) and continental crust (Dahlquist et al., 2010, 2021; Macchioli Grande et al., 2020). This retro-arc plutonic magmatism is accompanied to a lesser extent by bimodal volcanic successions composed of rhyolites-trachytes and alkaline basalts and alkali basaltic and lamprophyric dykes (Alasino et al., 2012; Coira et al., 2016; Martina et al., 2018). Therefore, the Devonian foreland and retro-arc Carboniferous magmatism developed in the intracontinental region (present-day Eastern Sierras Pampeanas, Fig. 1) was mainly continuous from ca. 390 Ma to ca. 320 Ma, although important geochemical and isotopic compositional variations occurred through time and space linked with distinctive tectonic regimes (Dahlquist et al., 2018). In general, the host rocks of these granitoids are dominantly migmatites and gneisses developed during the Early Paleozoic orogenies (Pampean and Famatianian) and Ordovician granitoids (Famatinian orogeny), overprinted by marked shear deformation yielding major mylonitic belts (Dahlquist et al., 2021; Larrovere et al., 2016).

3. Field occurrence and lithology descriptions

Our study was carried out on two representative intrusive complexes of Early Carboniferous age and A-type composition which outcrop in the Eastern Sierras Pampeanas of Catamarca province (Figs. 1 and 2): Vinquis intrusive Complex and Zapata intrusive complex. Although the main objective of this research is to study the petrogenesis of the Andaluca Unit that belongs to the Vinquis intrusive complex. The Andaluca Unit and surrounding rocks of the Vinquis and Zapata Inclusive Complexes were mapped and sampled for geochemical and geochronological analyses. A detailed description of field with the studied geological cross-sections, their petrography and contact relations is detailed the Supplementary Material 1. Also, Supplementary Material 2 provides a summary of the petrography of the studied units and the collected samples, as well as the main data of mineral chemistry.

3.1 The Vinquis Intrusive Complex

Morales Cámera et al. (2017) described five granitic facies from the eastern and southern flanks of the Sierra de Vinquis in what they called the Vinquis batholith. With the aim of leaving aside terms that have genetic or size implications, taking into account the complexity of the magmatic bodies, and adapting the terminology to recent uses (e.g., Paterson et al., 2016; Alasino et al., 2017; Macchioli Grande et al., 2020), we rename here the Vinquis batholith to "Vinquis Intrusive Complex" (VIC), which comprises all the Devonian-Carboniferous magmatic units that form the Sierra de Vinquis. New mapping established that two main intrusive units form the VIC (Fig. 2), the older Vinquis Unit (VU) and the younger Andaluca Unit (AU).

3.1.1 Host rocks

The Vinquis Intrusive Complex (VIC), with an area of approximately 390 km^2 (Fig. 2), was emplaced in the Carboniferous retro-arc domain previously referred in a sector of the basement called the Central Famatinian Domain, which is largely dominated by I- and S-type granitoids of the Ordovician Famatinian magmatic arc (Rapela et al., 2018). The rocks of the local metamorphic basement crop out sporadically along its eastern flank as small scattered inliers in the modern sediments (Morales Cámera et al., 2017; Sosci, 1972) and as a larger outcrop in the northern end of the VIC (González Bonorino, 1972; Lazarte, 2013; Toselli et al., 1992) (Fig. 2). The dominant host rocks are fine- to very fine-grained biotite schists, medium-grained mica schists and quartz-biotite phyllites. They show penetrative foliation with frequent N-NW strike (305° to 331°) and subvertical to intermediate dip (ca. 70º SW), and in some places a thermal metamorphic overprint resulting in the formation of hornfels associated to the emplacement of the VIC (Lazarte, 2013; Sosic, 1972). Mylonitic granites (~340°/65°SW) appear sandwiched between the rocks described above (Morales Cámera, 2019). In some sectors, towards the interior of the eastern flank of the Sierra de Vinquis, the metamorphic rocks are formed by medium-grained banded migmatite gneisses (Qtz+Pl+Bt+Kfs+Ms), protomylonites (of granitoid protolith) and fine-grained schists. These metamorphic rocks form locally separated thin septa (metric to decametric) oriented 53°/60°NW showing a dominant steep N-NE foliation (5°/35°E - 55°/86°NW) within the VU granitoids.

3.1.2 The Vinquis Unit

The VU is composed by five dominant subunits that show an important areal development with visible or mappable contacts between them (Fig. 2) (Morales Cámera et al., 2017; Morales Cámera, 2019): A) Bt≈Ms porphyritic monzogranite to syenogranite; B) Ms≥Bt medium-grained equigranular syenogranite; C) Bt≈Ms fine-grained equigranular syenogranite; D) Ms>Bt porphyritic alkali feldspar granite, and E) porphyritic biotite monzogranite. The general magmatic mineral assemblage is Qz + Afs + Pl + Bt ± Ms with Ap + Zrn+ Mnz ± Ilm as accessories (mineral abbreviations from Whitney and Evans, 2010), with the occasional presence of magmatic garnet phenocrysts (Alm + Spes) in subunit B and tourmaline and sillimanite in subunit D (Morales Cámera et al., 2017).

According to these authors, the two-mica granites of the VU have a restricted SiO_2 range (71.5% to 74.8%) and are classified as a singular A-subtype with strongly peraluminous composition due to its high Ga/Al and Rb/Sr ratios, high Nb and P_2O_5 concentrations and high F content inferred from biotite compositions (average F = 1.17% wt.%). These geochemical signatures are also shared by the strongly peraluminous A-type granites of the late Devonian Achala batholith (Dahlquist et al., 2014; Morales Camera et al., 2020). The VU was emplaced in the latest Devonian or earliest Carboniferous time: 355 ± 7 Ma (U-Pb LA-MC-ICP-MS zircon age, B Subunit, Morales Cámera et al., 2017) and 353 ± 2 Ma (U-Pb LA-MC-ICP-MS zircon age, A Subunit, Sanematsu et al., 2018). The emplacement of the VU was synchronous with Early Carboniferous metaluminous A-type granites in the pre-Andean retro-arc region of SW Gondwana (357 ± 3 to 322 ± 3 Ma) (Dahlquist et al., 2013, 2021).

3.1.3 The Andaluca Unit

The Andaluca Unit (AU) defines a semi-elliptical plutonic body with an outcrop area of approximately 60 km^2 located in the southwestern part of the VIC (Fig. 2). It is composed of three dominant rock types, from north to south: (i) medium grained porphyritic biotite syenogranite with abundant microcline phenocrysts (5.0 × 5.0 - 2.8 × 1.1 cm) enclosed in a medium- to coarse-grained equigranular matrix formed by quartz, feldspars and biotite (Fig. 3a); (ii) coarse-grained porphyritic quartz monzonite with abundant microcline phenocrysts (6.0 × 5.0 - 6.0 × 2.8 cm) in a coarse-grained equigranular matrix of plagioclase, quartz and biotite (Fig. 3b); and (iii) white porphyritic alkali feldspar granite with abundant microcline phenocrysts (5.0 × 2.3 - 3.0× 0.7 cm) enclosed in a coarse-grained equigranular matrix containing pods formed by biotite and garnet (Fig. 3c). Internal contacts between these lithologies were not identified.

A fabric defined by the alignment of microcline phenocrysts is observed and interpreted as magmatic in origin. The dominant orientation of microcline phenocrysts is ~347°/80° SW in the quartz monzonite and ~315°/55°SW in the syenogranite. Also, concentric open schlieren (i.e., troughs) and weak layer schlieren of cm to metric dimensions, formed mainly by biotite and accessory minerals such as zircon, apatite and opaque minerals, were identified. The AU includes numerous enclaves, many of which are concentrated in the center of the unit: (i) metre to decameter-scale ellipsoidal to irregular grey medium to coarse-grained porphyritic intermediate granitoids (Fig. 3d); (ii) isolated decimetre-scale aphanitic dark grey subvolcanic ovoid rocks (Fig. 3e); (iii) meter to decameter-scale light orange medium to coarse-grained porphyritic biotite monzogranite with angular to ovoid shapes and sharp, straight to irregular contacts (Fig. 3f); (iv) isolated and scarce irregular meter- to decimeter-scale pink mylonitic granitoids displaying sharp and irregular contacts.

The contact between the AU and the granitic host rock of the VU could not be fully seen due to the steep terrain and the few accesses to these regions. In the northern region of the AU, the AU cut sharply the dominant magmatic foliation of the host subunit E of VU ($S_{magmatic}$ ranging from 225°/83°W to 272°/52°

NE) (Fig. 3g). Also, metre-scale irregular dykes of the AU intrude into a host equigranular biotite syenogranite (Fig. 3h) and separates blocks of this rock, suggesting that the northern region of the AU represents the roof of the pluton.

3.2 The Zapata Intrusive Complex

The Zapata Intrusive complex (ZIC) is a very extensive granitic body cropping out in the Sierra de Zapata next to the western flank of the Sierra de Vinquis. The AU and the ZIC are separated by the modern fault that raised the Sierra de Zapata (Fig. 2). The metamorphic rocks are very scarce in this mountain range, appearing as small outcrops of biotitic gneisses in the modern sediments (Dahlquist et al., 2010). The dominant rock types of the ZIC are porphyritic biotite monzogranite to syenogranite with large microcline crystals (5.0 to 3.6 cm long) set in a coarse-grained or fine-grained matrix with zircon, monazite, apatite, Fe-Ti oxides ± amphibole and epidote as accessory minerals (Dahlquist et al., 2010). In the southern end of the mountain range, crops out of two-mica and biotitic medium-grained porphyritic granites (considered equivalent to subunits A and E of VU, respectively) and of porphyritic two-mica (biotite >> muscovite) syenogranite with abundant microcline phenocrysts enclosed in an inequigranular medium to fine matrix with can be recognized. This last syenogranite intrude a shear-deformed coarse-grained porphyritic biotite granitoid with microcline megacrysts (10.0 × 4.0 - 4.5 × 1.5 cm) ($S_{mylonitic}$ =100°/65°S - 75°/49°S) to the west, similar to the Ordovician porphyritic meta-granodiorites that crop out extensively in the nearby Sierra de Copacabana (Höckenreiner et al., 2003), showing a sharp contact (175°/82°W) and irregular xenoliths of the deformed granite. To the east, the Zapata syenogranite intrudes the equivalents peraluminous rocks of subunits E and A of VU. The contact is sinuous and sharp, with tabular dykes of variable thickness (0.5 and 3 m) of the Zapata syenogranite intruding the VU.

The dominant biotite granites of the ZIC have a high and restricted range of SiO_2 (71.9% to 75.6%) and are classified as metaluminous to weakly peraluminous A-type granites (Dahlquist et al., 2010), emplaced at the earliest Carboniferous as indicated by the U-Pb LA-MC-ICP-MS zircon age of 340 ± 3 Ma reported by Dahlquist et al. (2013) for a porphyritic granite.

4. Element and isotopic geochemistry

For this study, whole-rock major and trace element compositions of 19 rocks from AU, VU and ZIC described in the previous section were analyzed (Fig. 2; Table 1). Nine representative samples from each unit have also been analyzed for Nd and Sr isotopes (Table 2). Mineral compositions (Supplementary Material 3) were determined in three samples of the AU (VIN-203, VIN-114, VIN-92) and one of the ZIC (VIN-101) and are descripted in the Supplementary Material 4. For U-Pb zircon dating, zircon grains were separated from the quartz monzonite (VIN-200) and the alkali feldspar granite (VIN-202) of the AU and

a two-mica alkali feldspar granite (VIN-18) from the VU (Table 3). On zircons from the dated samples, Hf isotope data were obtained (Table 4; Supplementary Material 5). Detailed information about the analytical methods is given in the Supplementary Material 6. The relative proportions of constituent minerals of each sample were quantified by mass balance calculations from mineral chemistry data from representative samples (Supplementary Material 7).

4.1 Whole-rock geochemistry

4.1.1 Major elements

The AU contains SiO_2-poor (68.5% - 69.8%) and SiO_2-rich (73.4% - 76.0%) lithologies that correspond to the quartz monzonitic and granitic varieties described above. The SiO_2-rich rocks, together with the granitic rocks of the VU (SiO_2 = 70.1% - 75.1%), plot close to the limit between midalkaline and subalkaline fields of the TAS diagram of Middlemost (1994) (Fig. 4a). The granitoids of the ZIC studied in this work plot in the midalkaline granite field and resemble the Carboniferous metaluminous to weakly peraluminous A-type granites of the Sierras Pampeanas.

The P-Q multicationic classification of Debon and Le Fort (1988) is a measure of quartz abundance and an indication of the proportion of K-feldspar among feldspars. Most granitoids plot mainly in the granite field indicating similar proportions of plagioclase and alkali feldspar and enrichment in quartz (Fig. 4b). The SiO_2 poor-granitic rocks (quartz monzonites) of the AU plot close to the limit between granite and quartz syenite fields. The granitoids of the AU and some of the ZIC have a higher P value than VU indicating an enrichment of K-feldspar.

Aluminum saturation index (ASI) was calculated according to Zen (1986) (molar Al_2O_3 / [(CaO– 3.33 × P_2O_5) + Na_2O+K_2O]) but the categories of peraluminous granites are according to Clarke (2019). The AU and ZIC granitoids are metaluminous to weakly peraluminous, with ASI ranging from 0.99 to 1.10 (Fig. 4c). The latter are similar to the Early Carboniferous metaluminous A-type granites (including the northern region of the Sierra de Zapata) reported by Dahlquist et al. (2010), whilst the VU granitoids are moderately to strongly peraluminous (ASI = 1.12-1.39).

In the A-B diagram of Debon and Le Fort (1988) modified by Villaseca et al. (1998) (Fig. 4d) the granitoids of the AU define a negative slope trend from the field of felsic peraluminous to low peraluminous granites, similar to the trends of the granitoids from southern ZIC and other Early Carboniferous A-type granites of the Sierras Pampeanas. The VU granitoids show a slightly positive slope in the field of felsic peraluminous granites that bends to a marked negative slope in the field of the moderately peraluminous granitoids.

Like the Carboniferous metaluminous A-type granitoids of the Sierras Pampeanas, the AU and ZIC rocks plot in the ferroan field in the $FeO^t/(FeO^t+MgO)$ (Fe*) vs. SiO_2 diagram of Frost et al. (2001) (Fig. 4e), whereas the VU granitoids plot in the magnesian field within the compositional range of A-type granites. In all rock groups an increase in Fe* is observed with increasing SiO_2 content. The AU and ZIC rocks cross the alkali and alkali-calcic trends in the Na_2O+K_2O-CaO vs. SiO_2 diagram of Frost et al. (2001) (Fig. 4f), while the VU granitoids follow the boundary of the alkali-calcic and calc-alkalic trends.

In variation diagrams based on TiO_2 content, very useful to visualize compositional trends within SiO_2-rich granites, well-defined trends for several major elements can be observed (Fig. 4g). The SiO_2 shows negative correlations for all samples, while CaO, K_2O, FeO^t and MgO show positive correlations. The Al_2O_3 shows a well-defined positive correlation in AU granitoids, whereas the VU granites show a flat or a very slightly positive trend. The P_2O_5 content show positive correlation for the different granitic units. For the same TiO_2 content, the AU and the ZIC are enriched in CaO, K_2O, FeO^t and depleted in MgO and P_2O_5 compared to the VU.

4.1.2 Trace elements

The quartz monzonite of the AU is characterized by a moderate REE slope with an enrichment in the LREE content relative to HREE (La_N/Yb_N = 9.45-12.65) and slightly negative Eu anomalies (Eu/Eu* = 0.55-0.62) (Fig. 5a). Conversely, the SiO_2-rich rocks of the AU have a flat REE pattern slope or a slight LREE enrichment (La_N/Yb_N = 3.28-7.69), displaying significant negative Eu anomalies (Eu/Eu* = 0.10-0.22) (Fig. 5a). These REE patterns are similar to those of the Early Carboniferous metaluminous A-type granites of the Sierras Pampeanas (Dahlquist et al., 2010). The VU is characterized by a moderate slope with a slight enrichment in the LREE content relative to HREE (La_N/Yb_N = 4.85-19.88) and a marked negative Eu anomaly (Eu/Eu* = 0.34-0,50). REE patterns similar to those of the VU granitoids are observed in the granitoids of the ZIC (La_N/Yb_N = 11.64-7.67; Eu/Eu* = 0.41-0.43) (Fig. 5b).

The patterns in the primitive mantle-normalized spider diagrams (Fig. 5c-d) are similar for the different units, with marked negative Ba, Nb, Sr, Eu and Ti anomalies, significant enrichment in Cs and Rb, and moderate enrichment in Th and U. Some High Field Strength Elements (HSFE) (i.e., REE, Y, Zr, Hf) are enriched in the weakly peraluminous AU and the ZIC compared to the strongly peraluminous granites of the VU. There exists a strong inverse correlation between the concentration of HFSE and the ASI, with the metaluminous to weakly peraluminous granites showing high HFSE contents comparable to those of classical A-type granites (e.g., Zr+Nb+Ce+Y >350 ppm) (Fig. 5e).

In the bivariate diagrams against TiO_2 (Fig. 6), the AU granitoids display well-defined negative trends for HREE, Y, Rb and U, slightly positive trends for LREE, Th and Nb and marked positive trends for Zr, Sr, Ba, Eu and V with increasing TiO_2. The VU shows positive trends for Ba, Sr, LREE, Th, HREE, Y, Eu, Zr, Y and V, poorly positive trends for Nb and roughly negative trends for Rb and Cs. At constant TiO_2 content, the AU granitoids are richer in most trace elements than

the VU granitoids. The samples of the ZIC, in general, do not show defined trends but they closely resemble the behaviour of the Early Carboniferous metaluminous A-type granites of the Sierras Pampeanas.

4.2 Whole-rock Sr-Nd isotopes

The quartz monzonite of the AU and the hosted schlieren have εNd_t of −2.95 and −2.62, respectively, whereas the SiO_2-rich granites have slightly lower εNd_t values (−3.49 - −3.65), within the range of the values reported by Dahlquist et al. (2013) for the Early Carboniferous metaluminous A-type granites (εNd_t = +2.10 - −4.69) (Fig. 7). The new εNd_t values of the strongly peraluminous granite of the VU (εNd_t = −5.31 - −6.34) are similar to those previously reported for the same unit (εNd_t = −6.11 - −8.09) (Morales Cámera et al., 2017) and significantly lower than those of the AU.

The quartz monzonite and syenogranite of the AU yielded $^{87}Sr/^{86}Sr_t$ values of 0.7092, and 0.7140, respectively. The alkali feldspar garnet-bearing granite showed an anomalous value of 0.6970 (Fig. 7). The strongly peraluminous granites of the VU yielded $^{87}Sr/^{86}Sr_t$ values between 0.7140 and 0.7211, similar to values previously reported by Morales Cámera et al. (2017) (0.7170 - 0.7275). The equigranular biotite syenogranite (sample VIN-105) of the western VU yielded $^{87}Sr/^{86}Sr_t$ = 0.7165 and εNd_t = −5.06.

4.3 Zircon U-Pb geochronological and Hf isotopic constraints

4.3.1 U-Pb zircon SHRIMP ages

U-Pb analyses were mostly located in outer zones of the zircon crystals to define the crystallization ages. Zircon grains of the studied samples are mostly prismatic and elongated (VIN 200 = 160 × 55 - 300 × 100 µm; VIN-202 = 145 × 60 - 300 × 90 µm; VIN-18 = 335 × 120 - 135 × 50 µm) with subhedral to euhedral terminations and dominant oscillatory zoning (Table 3; Figs. 8a-c).

Eleven analyses were performed on zircons from sample VIN-200 of the quartz monzonite from the AU, yielding concordant analyses. Using the technique proposed by Siegel et al. (2018) (after Sinclair, 1974) to define analyses as outliers by a cumulative probability plot, two data points were excluded in the age crystallization calculation (391± 9 Ma and 361 ± 4). The other nine analyses give a Tera-Wasserburg concordia age (Vermeesch, 2018) of 344 ± 3 Ma (MSWD = 0.13) and yield a weighted mean age of 344 ± 3 Ma (MSWD = 1.31). However, excluding analyses with high uncertainties we obtain a concordia age of 346 ± 3 Ma (MSWD = 0.077, n = 5) and a better weighted mean age of 346 ± 4 Ma (MSWD = 0.86, n = 5) (Fig. 8a), which are considered the best estimate for the crystallization age of the quartz monzonite.

Eleven analyses were performed on zircons from sample VIN-202 of the alkali feldspar granite from the AU, yielding concordant analyses. The visual inspection of the cumulative probability plot suggests that at least two discrete age populations may be present. The main and older population give a Tera-Wasserburg concordia age (Vermeesch, 2018) of 342 ± 3 Ma (MSWD = 0.24, n = 7) and a weighted mean age of 342 ± 4 Ma (MSWD = 0.87, n =7) (Fig. 8b). One analysis with high uncertainty was excluded in the crystallization calculation of this age. Younger ages (322 ± 4, 329 ± 8 and 331 ± 3 Ma) are presumed to reflect a Pb-loss and are not taken into account to calculate a meaningful age.

Zircons of the sample VIN-18 corresponding to the VU (D Subunit) yield abundant inherited Early Palaeozoic ages (n = 5, ranging from 525 to 483 Ma). Four individual analyses yield an inherited Late Cambrian Tera-Wasserburg concordia age of 491 ± 5 Ma (Fig. 8c). The magmatic zircons yield Devonian-Carboniferous ages. Four points give a Tera-Wasserburg concordia age of 363 ± 4 Ma (MSWD= 0.8, and a weighted mean age of 363 ± 6 Ma (MSWD= 1.75) which we interpret as the crystallization age of the strongly peraluminous alkali feldspar granite (Fig. 8c). One analysis leads to higher MSWD value (2.9) for the weighted mean and was excluded for the age crystallization calculation.

4.3.2 Hf in zircon isotope data

Hf in zircon isotope data for the three dated samples from the VIC are reported in Table 4 and Fig. 9. Zircons from samples VIN-200 and VIN-202 shown negative εHf_t (t = 345 and 342 Ma) values ranging from −16.48 to −7.68 and −8.54 to −3.26, respectively. The magmatic zircons from sample VIN-18 yield extremely negative εHf_t (t = 363 Ma) values of −37.73 and −18.21. Furthermore, inherited zircons have a markedly negative εHf_t (t = 498-483 Ma) values of −38.18 and −19.28. The two-stage continental age model (TDM) yield average of 2.1 Ga, 1.7 Ga, and 3.2 Ga, for the magmatic samples VIN-200, VIN-202, and VIN-18, respectively.

4.4 Mineral chemistry of biotite and melt fluorine and chlorine contents

4.4.1 Biotite composition

Biotite in the studied samples is iron rich (FeO > 26 wt.%) with very low atomic Mg/(Mg + Fe_{total}) of 0.06-0.25, mostly showing annitic compositions (Fig. 10a). Fluorine content is variable (0.45-1.52 wt.%) with the ZIC syenogranite showing the lowest contents (0.45-0.81 wt.%), whereas the AU syenogranite show slightly higher values (0.69-1.08 wt.%), and the quartz-monzonite and alkali feldspar granite from the AU show the highest values (0.98-1.52 wt.%). In the studied rocks, chlorine is lower than fluorine, showing values mostly lower than 0.4 wt.%, with the ZIC syenogranite showing the lowest values (<0.1 wt.%) and the AU alkali feldspar granite the highest (0.26-0.41 wt.%).

In the MgO–FeO–Al_2O_3 diagram from Abdel-Rahman (1994) (Fig. 10b), mica compositions from the ZIC syenogranite and the AU quartz-monzonite lie in the field of alkaline granitoids, whereas those from the AU syenogranite and alkali feldspar granite lie in the field of peraluminous granitoids. In the TiO_2–FeO–MgO diagram of Nachit et al. (2005), most of the analyses plotted in the field of the primary magmatic biotite (Fig. 10c). However, analyses from the alkali feldspar granite of the AU plot in the fields of reequilibrated and neoformed biotites suggesting late crystallization and interaction with late- to post-magmatic fluids, respectively (Nachit et al., 2005). Although the interaction with late- to post-magmatic fluids could have changed the F composition of the biotite of the AU alkali feldspar granite, the fact that the F contents are similar to those showed by the primary biotite indicate that the F was not affected by the referred fluids.

4.4.2 Melt fluorine and chlorine contents

Whole-rock fluorine and chlorine data are not available from the studied samples. However, the relatively high F contents of biotite, along with their very high atomic Fe/(Fe + Mg) ratios (>0.75) (Fig. 11a), strongly suggests that the magmas had relatively high HF/H_2O ratios. To determine the F and Cl content of the magma, given their importance in A-type magmas (e.g., Collins et al. 1982; Wang et al. 2018), the equations of Muñoz (1992) will be used. These equations were chosen due to the consistent results obtained previously in metaluminous to weakly peraluminous A-type granites (see Dahlquist et al., 2010) In particular, the atomic ratio Mg/(Mg + Fe + Mn) < 0.22 of the biotite are outside the range values used to calibrate the equations of London (1997) and cannot be used here.

The calculated F contents (Fig. 11b; Supplementary Material 6) are relatively high, with the ZIC granitoids showing values of 1278-2403 ppm, which are higher than those previously reported for this intrusive complex (F = 580 to 1180 ppm; Dahlquist et al., 2010), and the AU granitoids showing generally higher values (1950-5700 ppm). These values are within the calculated F contents range of the Carboniferous metaluminous A-type granites of Sierras Pampeanas (F = 580 to 5600 ppm; Dahlquist et al., 2010) and similar to the range of F analyzed in the Carboniferous metaluminous A-type Los Árboles pluton (or Los Ratones pluton) (500-8100 ppm, average 3825 ppm; De la Hoz et al., 2014). Using the equations of Muñoz (1992) for this pluton, the calculated F value is similar to the analyzed values (av. 4361 ± 368 ppm, Supplementary Material 7), supporting the calculations made for the ZIC and AU. The calculated Cl content is lower than the F content but still relatively high, ranging between 160 and 260 ppm in the ZIC granitoids and between 400 and 1090 ppm in the AU granitoids. These values overlap those reported by Dahlquist et al. (2010) (90 to 1050 ppm) for the Carboniferous metaluminous A-type granites from Sierras Pampeanas. Finally, the strongly peraluminous granitoids of the VU have F and Cl contents in the range of previous granitoids (F: 949-3525 ppm, Cl: 31-292 ppm).

5. Discussion

5.1 Geochronological context of the Vinquis Intrusive Complex magmatism

Based on a large U-Pb zircon geochronological dataset, Dahlquist et al. (2018, 2021) indicated that the Devonian-Carboniferous magmatism in Sierras Pampeanas was mainly continuous from ca. 390 Ma to ca. 320 Ma. According to the geochronological data of this work and of previous investigations, the magmatism in the Sierra de Vinquis was developed during the Mississipian. The zircon U-Pb ages for the granitoids of the VU (355 ± 7 Ma, B subunit, Morales Cámera et al., 2017; 353 ± 2 Ma, A Subunit, Sanematsu et al., 2018; 363 ± 5 Ma (VIN-18), D Subunit, this paper), the AU (between 346 ± 3 Ma and 342 ± 3 Ma, this paper) and the ZIC (340 ± 3 Ma; Dahlquist et al., 2013) indicate that the AU and ZIC rocks were contemporaneous and were emplaced 10-15 Ma after the VU rocks, in agreement with the intrusive nature of AU and ZIC into the VU (Section 3.1). Thus, as described above, the set of ages define two main magmatic events in this region: ~ 359 Ma and ~ 344 Ma, respectively. The first magmatic event is predominantly represented by moderately to strongly peraluminous A-type granites, whereas the second event is characterized by metaluminous to weakly peraluminous A-type granites.

Comparable age sets were identified in the studied metaluminous to weakly peraluminous A-type granitic units that crop out in the nearby Sierra de Velasco (Fig. 1). In particular, the Sanagasta Unit of the Huaco Intrusive Complex (HIC) registered a long magmatic activity (Macchioli Grande et al., 2020) with three groups of ages: 353 ± 5 Ma (Early Mississippian - Tournasian), 369 ± 5 Ma (Late Devonian - Famennian) and 378 ±2 Ma (Late Devonian - Frasnian), spanning an age range similar to the first event recorded in the Sierra de Vinquis. Based on these geochronological data and structural studies, Macchioli Grande et al. (2020) concluded that the younger age is considered the final crystallization, whereas the older Late Devonian ages could indicate recycling of antecrystic zircons formed during early magma crystallization during the construction of a long-lived magma reservoir.

The second and youngest magmatic event (ca. 344 Ma), is also recorded in the San Blas Intrusive Complex (SBIC), NW Sierra de Velasco (Fig. 1) (Alasino et al., 2017). This intrusive complex is composed by two main units: i) tabular to funnel-shaped intrusion composed of crustal-peraluminous two-mica granitoids (Asha Unit, 340 ± 7 Ma) and ii) cylindrically-shaped intrusion composed of multiple smaller magma batches with a metaluminous to weakly peraluminous composition and a more primitive isotopic signature (San Blas Unit, 344 ± 2 Ma). Alasino et al. (2017) concluded that this intrusive complex was formed by multiple non-consanguineous incremental magmatic intrusions that used the same magmatic plumbing system during ascent. These authors postulate that lower crust-derived magmas were involved at the beginning, with subsequent and variable mixing with partial molten material derived from the subcontinental mantle. These magmas gradually moved upwards by taking advantage of pre-heated channel pathways of the previous intrusions.

Based on the geochemical and geochronological data presented here, we postulate that the granites of the VIC have a similar thermal history to that described for the nearby Sierra de Velasco granites, with a long-lasting magma reservoir developed by multiple non-consanguineous incremental magmatic intrusions that used the same magmatic plumbing system during ascent. In addition, the steep contacts between the VU and the metamorphic wall rock, the local separation of the VU granitoids by thin septa of host rock, and the steep magmatic foliation, suggest an emplacement model of initial magma wedging of sheet-like bodies that evolved to amalgamated magma bodies. The magma of the AU probably ascended as an elongated viscoelastic body in a thermally mature region, as reported for similar cylindrical-shaped intrusions in the region (Alasino et al., 2017; Macchioli Grande et al., 2019). However, detailed structural studies are required to be more conclusive.

5.2 Source of magmas from isotopic data

5.2.1 Strongly peraluminous magmas

Morales Cámera et al. (2017), based on the geochemical compositions and isotope data (εHf and εNd) and inherited zircon ages, made some inferences regarding the source rocks of the VU granitoids. Because of the high inherited Ordovician and Cambrian zircon ages, crustal isotopic signature (εHf_t = −9.5 to −1.5 (av. −6.09) and εNd_t= −6.13 to −8.06 (av. −7.24)) and moderate to strong peraluminosity, the authors suggested a dominantly metasedimentary source for the parental magmas of the VU rocks. Figures 12a-c show the new and previous whole-rock Sr, Nd and Hf zircon isotope data of the studied rocks, as well as those of the dominant groups that constitute the pre-Carboniferous basement of the Eastern Sierras Pampeanas: i) sedimentary to metasedimentary rocks of the Puncoviscana Series, ii) sedimentary to metasedimentary rocks of the Post-Puncoviscana Series, iii) Ordovician S-type granitoids and iv) Ordovician I-type granitoids. The three isotopic systems show that all the moderately to strongly peraluminous samples from the VU are comparable to the pre-Carboniferous basement of the eastern Sierras Pampeanas (Figs. 12a-c), which is consistent with an origin involving melting of equivalent rocks. In addition, inherited Ordovician and Cambrian zircon ages were obtained from new and previously dated samples, VIN-18 and VIN-1, respectively. Cambrian and Ordovician ages are widely recognized in the surrounding basement of the Sierra de Vinquis (e.g., Larrovere et al., 2021; Rapela et al., 2016, 2018), suggesting that this basement was part of the source of the magmatism. Morales Cámera et al. (2017) concluded that the dominant εHf_t values of sample VIN-1 can be explained by $^{176}Hf/^{177}Hf$ transfer from Cambrian and Ordovician inherited zircon to magmatic zircons crystallized in the granites of the VU: zircons from exposure meta-sedimentary basement (Pampean and post-Pampean) (Fig. 12c) or some Famatinian S-type granites (e.g., Cerro Toro tonalite and Belen monzogranite) have highly negative εHf_t values (−22 to −14, Rapela et al., 2018). Similarly, when the εHf_t of Ordovician inherited zircons from sample VIN-18 are calculated at t = 363 Ma (−22.0, −37.9 and −40.5), the obtained values are comparable to those reported for zircons that crystallized at

the age of reference (−18.6 and −37.8). The most direct interpretation is that the strongly peraluminous magmas of the VU mainly resulted from the reworking of supracrustal material.

5.2.2 Metaluminous to weakly peraluminous magmas

Dahlquist et al. (2010, 2013) concluded that early Carboniferous metaluminous to weakly peraluminous A-type magmas resulted in part from the reworking of supracrustal material in a largely cratonized region, but with variable contribution of juvenile or subcontinental mantle magmas according to Macchioli Grande et al. (2020). The ZIC granitoids were part of the group of igneous bodies studied by these authors that show a more radiogenic crustal Nd-isotopic signal (εNdt = −3.74 to −2.54, average −3.18) than those of the Ordovician granitoids at the same time (−4.3 to −8.5, data from Dahlquist et al., 2010). The weakly peraluminous granitoids of the AU have similar εNd_t and $^{87}Sr/^{86}Sr_t$ values to those reported for the ZIC (Figs. 12a-b; Table 2). Likewise, they have a more radiogenic Nd isotopic signature and a lower initial Sr isotopic signature compared to the rocks of the pre-Carboniferous basement (Figs. 12a-b), suggesting a more primitive component in the source of these rocks.

The εHft values for the AU (ranging from −16.48 to −7.68) and ZIC (ranging from -12.82 to −4.00) granitoids are in the range of values of the crustal basement (Fig. 12c). However, as previously discussed, the rocks geographically closest to the AU with a dominant crustal origin, such as VIN-18, have a highly negative εHf_t signature (−18.6 to −37.8). Therefore, a mixing between a primitive and a crustal component could also explain the Hf isotopic signature of the AU and ZIC rocks.

The best approximation to the primitive component of the Carboniferous A-type magmatism are the expositions of coeval mafic magmatism in the region. This is composed of: (i) Mississippian retro-arc bimodal volcanic magmatism (Martina et al., 2011; Zappettini et al., 2015) composed by alkaline (shoshonitic) basalts with features comparable with transitional MORB and within-plate tholeiites and alkaline trachytes (Coira et al., 2016); (ii) alkaline (shoshonitic to high-K calc-alkaline) mafic dykes classified as back-arc basaltic trachyandesite to trachy-andesite (Alasino et al., 2012); and (iii) lamprophyre dyke swarms classified as K-rich calc-alkaline basalts of primary origin (Martina et al., 2018). The rocks of the groups (i) and (ii) have relatively low positive isotopic compositions (εNd_t = +3,32(i) - +2,10(ii); $^{87}Sr/^{86}Sr_t$ = 0,70429(i)-0,70463(ii); Coira et al., 2016; Alasino et al., 2017), when these isotopic values are compared with isotopic depleted mantle values (εNd_t = +10,45; $^{87}Sr/^{86}Sr_t$ = 0,70209; Allègre, 2008), enriched mantle values (EM1: εNd_t = −2,8; $^{87}Sr/^{86}Sr_t$ = 0,70514; EM2: εNd_t= −7,1; $^{87}Sr/^{86}Sr_t$ = 0,70764; Ernst and Buchan, 2003) and dominant subcontinental lithospheric mantle (SCLM) values estimated for this region of southwestern Gondwana (εNd_t = −4,68; $^{87}Sr/^{86}Sr_t$ = 0,70957; Alasino et al. (2020)) (Fig. 7). These data suggest that the primitive component of the A-type Carboniferous magmatism was composed of a hybrid between SCLM and asthenospheric mantle.

To quantify the mantle-crust ratio in the source of the AU granitoids, isotopic mixing calculations (following Faure, 1986) were performed. Due to the wide variability of Hf isotopic data in crustal rocks of the pre-Carboniferous basement, up to more than 50 epsilon units in some cases, it is hard to define an end-member close to the real one. Furthermore, the range in Sr is also difficult to quantify because of the high susceptibility of the Rb-Sr system to be disturbed by subsequent thermal processes or even by Sr remobilization caused by deuteric alteration common in evolved magmatic systems (e.g., Montero et al., 2009). Therefore, Nd isotopes were considered the most reliable data to use in calculations. As crustal members, the average of each group of the basement was used (Figs. 12a-c), discarding Ordovician I-type granitoids because there are no exposures of these rocks with strongly negative εHf_t values. As the mantle component, the previous referred samples of the Early Carboniferous mafic igneous rocks were used. The results indicate that between ~25% and ~ 50% of mantle-derived components contributed to the generation of the AU granitoids (Supplementary Material 9).

5.3 Interpretation of the whole-rock geochemical data of the AU and its relationship with the mafic magmatism

Based on the data reported in this work, the AU rocks have petrological and geochemical characteristics of A-type granitoids (following Bonin, 2007). The AU granitoids have an iron-rich mafic mineralogy composed of annitic biotite and almandine garnet, particularly in alkali feldspar granites. The bulk-rock compositions indicate a ferroan and alkali-calcic to alkalic affinity (Fig. 4e-f) with high LILE+HFSE abundances (Zr+Nb+Ce+Y > 350 ppm and a high Ga/Al ratio, Figs. 5e and 13a), plotting in the field of A-type granites on the discrimination diagrams of Whalen et al. (1987) (Fig. 13a). On the Rb vs Y+Nb tectonic discriminant diagram of Pearce et al. (1984), the AU rocks plot in the field of within-plate granite (WPG) (Fig. 13b). According to the three-fold subdivision of Eby (1992), AU granitoids belong to the A_2 sub-group (Fig. 13c). These patterns are similar to those reported for Early Carboniferous metaluminous A-type granites of Sierras Pampeanas (Dahlquist et al., 2010).

The coherent trends of SiO_2, Al_2O_3, FeO^t, MgO, CaO, K_2O, P_2O_5, Rb, Ba, Sr, Eu, Zr against TiO_2 (Figs. 4g and 6) would might suggest fractional crystallization as a dominant mechanism that explains the transition from quartz monzonite to extremely felsic granites of the AU (SiO_2 > ~72%) with a strongly fractionated composition (Rb > 336 and Sr < 70 ppm and Eu/Eu* < 0.22) by the crystallization of plagioclase, biotite, and K-feldspar, quartz with minor zircon, Fe–Ti oxides and apatite. However, the slight isotopic differences presented by the different AU lithologies (Sections 4.2 and 4.3.2) do not support exclusive fractionation processes. From this we interpret that the different lithologies represents batches of heterogeneous mixtures between mantle and crust components with different degree of fractional crystallization.

The common association between Carboniferous ferroan A-type granitoids of Sierras Pampeanas with the mafic dykes (Alasino et al., 2012; Dahlquist et al., 2010), as well as, the bimodal Carboniferous volcanic sequences constituted mainly by rhyolites and a lesser volume of basalts and trachytes (Coira et al.,

2016), suggest the participation of hot mafic magmas in the petrogenesis of these rocks. The Carboniferous mafic rocks plot dominantly in the Alkaline field on an alkali versus silica diagram (Fig. 14a) and trace element ratios as proxies for magma type (Nb/Yb vs. Th/Yb after Pearce, 2008) of these rocks indicate that the alkaline volcanites plots in E-MORB-OIB array (dominant uncontaminated magmas), whereas the alkaline dykes indicate some continental crustal involvement (Fig. 14b). All mafic rocks show an enrichment in the key trace elements (e.g., HFSE, REE, Ga) recognized in the A-type granitoids (Fig. 13a-c). This suggests that the A-type trace element signature of the granitoids may be associated with the previously enriched primitive component on the source. Although the enriched trace-element characteristics of alkaline basalts can be interpreted as derived from recycled oceanic crust with or without sediment, an alternative is that the enriched components are derived from recycled metasomatized lithospheric mantle (Pilet et al., 2008).

Another relationship between A-type granitoids and Carboniferous mafic rocks is the conditions of oxygen fugacity during crystallization. Early Carboniferous metaluminous to weakly peraluminous A-type granites of the Sierras Pampeanas have a strong ferroan signature, with high whole-rock ($FeO^t/(FeO^t + MgO)$ values (0.83–0.98) compatible with the reduced A-type granites (Morales Camera et al., 2017). It is widely known that reduced basaltic rock, such as alkali basalts, during differentiation are iron-rich because crystallization of magnetite is delayed (Frost and Frost, 2001). Thus, the ferroan signature of the granites under study may be genetically linked to the crystallization of reduced alkaline basaltic melts.

5.4 Volatile components (F and Cl) of the melts and the role of source rocks

A-type magmas are characterized by high halogen contents, especially F (e.g., Collins et al., 1982; Dahlquist et al., 2010; Eby, 1990; Moreno et al., 2014; Wang et al., 2018), which are believed to be crucial for the high concentration of HFSE in these magmas (Collins et al., 1982; Eby, 1990). However, F and Cl are not routinely analyzed in igneous rocks, whereby the contents are normally estimated from the measured F and Cl contents of F- and Cl-bearing minerals such as biotite and apatite (e.g., Dahlquist et al., 2010; Moreno et al., 2014).

The AU granitoids have high calculated whole rock F and Cl contents (F = 1950 to 5700 ppm; Cl = 400 to 1090 ppm), similar to those of the Carboniferous retro-arc metaluminous A-type granites of the Sierras Pampeanas (estimated F: 580-5600 ppm, estimated Cl: 90-1050 ppm; Dahlquist et al., 2010) (Fig. 11b), which in turn are clearly different from those of the Carboniferous calc-alkaline I-type granites from the Cordillera Frontal (estimated F: 0-355 ppm, estimated Cl: 250-630 ppm; data from Moreno et al., 2020, see Supplementary Material 8) and the Ordovician calc-alkaline I- and S-type granites from the Sierras Pampeanas (estimated F: 0-960 ppm, estimated Cl: 0-250 ppm; Dahlquist et al., 2010; Zandomeni et al., 2021), which represent arc magmatism (Fig.11b). The F-rich character of the Carboniferous retro-arc granites is also supported by the presence of fluorcarbonates and fluorite in the San Blas pluton and the La Chinchilla stock respectively (Grosse et al., 2009; Dahlquist et al., 2010) and by the high whole-rock F content in the Los Arboles (Los

Ratones) pluton (500 to 8100 ppm, average 3825 ppm) (De La Hoz et al., 2014). Thus, the F and Cl contents in these contrasting granitoids reflect differences in the nature of the parental magmas, as previously suggested by Dahlquist et al. (2010).

High F contents in A-type magmas have been explained by halogen and alkali rich fluids originated by mantle degassing causing metasomatism of the lithosphere (Bailey, 1980; Collins et al., 1982; Martin, 2006, 2012). This model proposes that the degassing of a rising asthenospheric mantle, in an extensional environment, releases alkaline fluids rich in H_2O + CO_2 and CH_4, with F, Cl, and assorted other species such as high field-strength elements and alkalis, which induce alkali metasomatism of the SCLM and granulitic lower crust (i.e., fenitization-type reactions). Likewise, these reactions transform the refractory intermediate to mafic rocks of the lower crust to fertile assemblages that can melt (in some cases completely according to Martin, 2006) to give A-type granitic magmas with a mixture of isotopic signatures from the recycled crust and the mantle.

On the other hand, fluorine usually behaves as an incompatible element in magmatic differentiation processes associated with crystal fractionation of essentially anhydrous assemblages (Kd<1), whereby high F contents could be reached for example after fractional crystallization of anhydrous minerals such as feldspars (Li et al., 2020; Sallet, 2000). Wang et al. (2018) have suggested that the elevated F contents in A-type granites may initially be originated from an F-rich melt and further elevated during prolonged magma differentiation.

Calculated F contents of the Carboniferous metaluminous to weakly peraluminous A-type granites of the Sierras Pampeanas are somehow comparable to those of A-type granites formed from crustal/mantle sources metasomatized by mantle-derived fluids such as: i) A-type granites from the Katerina Ring Complex (southern Sinai, Egypt; Moreno et al., 2014) (F = 960 to 10000 ppm, with the most evolved samples reaching very high values up to 30000 ppm), ii) A-type granites from the Galiñeiro Intrusive Complex (northwestern Spain; Montero et al., 2009) (F = 300 to 7200 ppm), and iii) A-type granites from the Derraman Peralkaline Felsic Complex in the West African Craton (Morocco; Bea et al., 2016) (F = 1300 to 1700 ppm) (Fig. 11b). Accordingly, the high fluorine of the Carboniferous retro-arc granites could be related to an alkaline and halogen-rich metasomatism of the upper mantle and probably the lower crust.

This halogen-rich metasomatism is compatible with the hybrid crustal-mantle signature of the AU (as discussed in Section 5.2.2). The F content of Carboniferous mafic rocks (and thus the F content of the initial mafic melts) can be estimated from their K_2O concentrations (Aoki et al., 1981, Ishikawa et al., 1980; Stecher, 1998). Considering the best fit-line for continental basaltic rocks reported by Aoki et al. (1981), the Carboniferous alkaline basalts of the volcanic successions (av. K_2O = 2.61 wt.%, Coira et al., 2016), alkaline basaltic dykes (av. K_2O = 3.18 wt.%, Alasino et al., 2012; Dahlquist et al., 2010) and lamprophyre dykes (K_2O = 1.74 wt.%, Martina et al., 2015) from NW Argentina would have high F contents, of around 920 ppm, 1100 ppm and 610 ppm, respectively. These values are similar to those of basaltic dykes related to the Carboniferous A-type Los Arboles (Los Ratones) pluton (1000 ppm), while an andesitic dyke had an anomalously high concentration of 5900 ppm (De la Hoz et al., 2014), which also support the high F present in these Carboniferous

magmatic mafic members that represent the primitive component discussed in Section 5.2.2. This indicates that the high fluorine of the A-type granitoids is related to their primitive component. Likewise, it supports the evidence in favor of a process of metasomatism in the SCLM source rocks.

On the other hand, the fluorine composition of the crustal component of the AU source can be inferred from the composition of the Carboniferous strongly peraluminous A-type granitoids of the VU, interpreted as derived from the pre-Carboniferous crust. The granites of VU have a high calculated whole-rock F and Cl content (estimated F: 949 to 3525 ppm, estimated Cl: 31 to 292 ppm; Supplementary Material 8), which suggest that the crustal component could also contribute high fluorine to the AU parental magmas.

5.5 Interaction between crustal rocks and mafic magmas for the origin of ferroan granitoids

Despite the isotopic, major and trace elements and field relationships between A-type granitoids and coeval mafic rocks, it was recognized that the fairly evolved composition and large volume of the all Carboniferous metaluminous to weakly peraluminous A-type retro-arc intrusive complexes (SiO_2 = 69.2-76.4 wt.%.; Dahlquist et al., 2010) including AU, are gapped from the composition of their contemporaneous to late isolated metric alkaline mafic dykes (SiO_2 = 50-64 wt.%.; Alasino et al., 2012). These gaps suggests that interaction between mafic magmas or variably evolved mantle-derived magmas and crustal rocks were insignificant process at the emplacement level of these intrusive complexes, being dominantly restricted to deep regions of the crust. However, the abundance of intermediate composition enclaves does not rule out that mingling and recharge processes may have occurred.

Experimental petrology shows that interaction of basaltic magmas with quartzo-feldspathic metasedimentary rocks at different pressures generate wide spectrum of high-SiO_2 melts in equilibrium with hybrid mafic cumulates. Segregation and ascent of the melts will give rise to shallow silicic magmas bearing evidence of a large mantle component, coeval with the consolidation, in the deep crust, of mafic granulites with evolved isotopic compositions (Patiño Douce, 1995). Parallel, on the origin of ferroan metaluminous to weakly peraluminous A-type granitoids, a petrogenetic model that has significant scientific consensus implies crustal assimilation with simultaneous fractional crystallization of relatively mafic magmas (Frost and Frost, 2011). On a regional scale, the dominant petrogenetic model postulated for the Early Carboniferous ferroan metaluminous to weakly peraluminous A-type magmatism of Sierras Pampeanas follows these ideas. Dahlquist et al. (2010) concluded that these magmas were originated primarily as mantle-derived magmas that suffered crustal contamination in variable proportions with subsequent and progressive fractional crystallization and dominant fractionation of feldspars. Alasino et al. (2017) agrees with this hypothesis to explain the origin of the metaluminous to weakly peraluminous A-type granitoids of the San Blas Intrusive Complex in the Sierra de Velasco. These authors consider that the parental magmas these rocks can be residual products of the fractionation of mafic magmas with some crustal assimilation and that initial partial melting in the lower crust could reflect underplating/intraplating of mafic magmas at the base of the crust in

a retro-arc setting. From the chemical and isotopic similarities found between AU granitoids and the rest of the Carboniferous ferroan granitoids (see section 5.3), a similar petrogenetic model that includes crustal assimilation and fractionation from mantle-derived magmas at a deep crustal level can be postulated.

5.6 Evidence from the geotectonic setting

During the development of the Late Devonian-Early Carboniferous magmatism an extensional regime is implanted in a retro-arc situation on a crust with prominent weaknesses (previous crustal shear zones) (Dahlquist et al., 2010), with the development of sedimentary basins (Ezpeleta et al., 2020) and exhumation and tectonic uplift process (Dávila et al., 2021). This geologic context has been interpreted in response to change in the tectonic plate configuration where in pre-Andean margin a roll-back led to 'normal' ocean slab subduction and convective hot asthenospheric mantle upwelling increased in the intracontinental region (Dahlquist et al., 2021). This environment prone to promoting heat transfer, metasomatic adjustment and melting processes between the mantle and the crust (Martin, 2012). Recently, Alasino et al. (2022), based on an extensive geochemical and U-Pb zircon age database, estimated that during the Mid-Late Devonian to Early Carboniferous retro-arc magmatism the thickness of crust changed from thick (>50 km at ~390 Ma) to moderate (40–50 km at ~340 Ma). The authors concluded that these thick crusts promote extensive fractionation processes and crustal contamination at deep and intermediate crustal levels, developing evolved magmatic compositions.

5.7 Petrogenetic models for the studied A-type granitoids

Based on all the previous evidence discussed, the following petrogenetic model is proposed for the rocks studied (Fig. 15). During Late Devonian the asthenospheric mantle upwelling in the retro-arc region produced significant degassing that metasomatizes and heats the thinned subcontinental lithospheric mantle (SCLM) and probably the lower crust, enriching them in alkalis, incompatible and refractory elements and modifying their isotopic signatures. Product of decompression and heating, partial mafic melts derived dominantly from the enriched SCLM tend to underplate/intraplate the base of the continental crust, transferring heat to it. In this stage (~365-355 Ma) the partial melting of the most fertile crust would take place, generating the VU parental magmas. As mantle upwelling progresses, large volumes of SCLM-derived alkaline magmas are density entrapment and underplating/intraplating in the deep crust, developing fractionation processes and assimilating variable volumes of preheated crust. In this stage (~345-340 Ma), the ferroan weakly peraluminous A-type parental magmas of the AU, and probably of the ZIC, are produced. Then, these magmas ascent as multiples batches (mostly non-consanguineous) by a same pre-heated pathway and intrude the VU.

6. Conclusions

1) Whole-rock chemical composition together with mineral chemistry and petrographic data indicate that the Andaluca plutonic unit is composed of F-rich ferroan weakly peraluminous A_2-type granitoids. Intrusive igneous rocks include: i) quartz monzonites, ii) syenogranites and iii) alkali feldspar granites.
2) This pluton was emplaced in earliest Carboniferous time (346 ± 3 Ma and 342 ± 3 Ma). The emplacement of this pluton was synchronous with Early Carboniferous metaluminous to weakly peraluminous A-type granites in the retro-arc region of SW Gondwana reported in previous works.
3) The host rocks are the moderately to strongly peraluminous A-type granites of the Vinquis Unit. The new U-Pb zircon crystallization age of the southern sector of this unit (363 ± 4 Ma) together with a previous age in the northern sector (355 ± 7 Ma) confirm that these granites were emplaced in the Devonian-Carboniferous boundary.
4) The geochemical A-type signature of Carboniferous metaluminous to weakly peraluminous granitoids (i.e., high F, HFSE, Ga/Al and ferroan and alkali-calcic to alkalic affinity) could be explained as derived from an F- HFSE- and alkali-rich parental mafic magma.
5) The petrogenesis proposed for the parental magmas of the metaluminous to weakly peraluminous A-type granitoids implies, in the first instance, the origin of F- HFSE-rich alkaline mafic magmas derived from the subcontinental lithospheric mantle previously metasomatized by degassing of the asthenospheric mantle. In a second instance, in a thick crust (>30 km), alkaline mafic magmas underplated/intraplated deep in the crust undergo crystal fractionation and crustal assimilation to form this variety of A-type granitoids.

Acknowledgment

Financial support for this paper was provided by Argentine public grants FONCyT PICT-2016 0843, FONCyT PICT-2018-1899, PIP0178 and PIP0564 CONICET, Consolidar 2018 SECyT-UNC, PUE 2016 N◦ 22920160100016 CONICET, Spain public grant CGL2016-76439-P, and a stay developed by JAD at the Geosciences Institute of the Sao Paulo University supported by grant FAPESP 2018/06837-3 (Sao Paulo State Foundation, Brazil) linked to Thematic Project (FAPESP 2015/03737-0). We thank José F. Molina Palma and Pablo H. Alasino for their very constructive reviews that significantly improved the manuscript and Aitor Cambesés for editorial assistance.

References

Abdel-Rahman, A.M., 1994. Nature of biotites from alkaline, calc-alkaline and peraluminous magmas. Journal of Petrology, 35, 525–541, https://doi.org/10.1093/petrology/35.2.525

Abdel-Rahman, A.F.M., Nassar, P.E., 2004. Cenozoic volcanism in the Middle East: petrogenesis of alkali basalts from northern Lebanon. Geological magazine, 141(5), 545-563.

Alasino, P.H., Dahlquist, J.A., Pankhurst, R.J., Galindo, C., Casquet, C., Rapela, C.W., Larrovere, M., Fanning, C.M., 2012. Early Carboniferous sub- to mid-alkaline magmatism in the Eastern Sierras Pampeanas, northwestern Argentina: a record of crustal growth by the incorporation of mantle derived material in an extensional setting. Gondwana Research 22, 992-1008.

Alasino, P.H., Larrovere, M.A., Rocher, S., Dahlquist, J.A., Basei, M.A.S.,Memeti, V., Paterson, S., Galindo, C., Macchioli, M., da Costa Campos Neto, M., 2017. Incremental growth of an upper crustal, A-type pluton, Argentina: Evidence of a re-used magma pathway. Lithos 284-285, 347-366.

Alasino, P.H., Casquet, C., Galindo, C., Pankhurst, R.J., Rapela, C.W., Dahlquist, J.A., Recio, C., Baldo, E.G., Larrovere, M.A., Ramacciotti, C.D., 2020. O-H-Sr-Nd isotope constraints on the origin of the Famatinian magmatic arc, NW Argentina. Geological Magazine 159(12), 2067-2080.

Alasino, P. H., Paterson, S. R., Kirsch, M., Larrovere, M. A., 2022. The role of crustal thickness on magma composition in arcs: an example from the pre-Andean, South American Cordillera. Gondwana Research 106, 191-210.

Allègre, C.J., 2008. Isotope geology. Cambridge University Press.

Aoki, K., Ishiwaka, K., Kanisawa, S., 1981. Fluorine geochemistry of basaltic rocks from continental and oceanic regions and petrogenetic application. Contributions to Mineralogy and Petrology 76, 53-59.

Augustsson, C., Willner, A. P., Rüsing, T., Niemeyer, H., Gerdes, A., Adams, C. J., Miller, H., 2016. The crustal evolution of South America from a zircon Hf-isotope perspective. Terra Nova, 28(2), 128-137.

Bailey, D.K., 1980. Volcanism, earth degassing and replenished lithosphere mantle. Philosophical Transactions of The Royal Society A: Mathematical Physical and Engineering Sciences 297 (1431), 309-322.

Bea, F., Montero, P., Haissen, F., Molina, J.F., Michard, A., Lazaro, C., Mouttaqui, A., Errami, A., Sadki, O., 2016. First Evidence for Cambrian Rift-related Magmatism in the West African Craton margin: the Derraman Peralkaline Felsic Complex. Gondwana Res. 36, 423–438.

Blichert-Toft, J., Albarede, F., 1997. The Lu-Hf isotope geochemistry of chondrites and the evolution of the mantle-crust system. Earth and Planetary Science Letters 148, 243-258.

Bonin, B., 2007. A-type granites and related rocks: evolution of a concept, problems and prospects. Lithos 97, 1-29.

Casquet, C., Dahlquist, J.A., Verdecchia, S.O., Baldo, E.G., Galindo, C., Rapela, C.W., Pankhurst, R.J., Morales Cámera, M.M., Murra, J.A., Fanning, C.M., 2018. Review of the Cambrian Pampean orogeny of Argentina; a displaced orogen formerly attached to the Saldania Belt of South Africa? Earth-Science Rev. 177, 209-225.

Cawood, P.A., 2005. Terra Australis orogen: Rodinia breakup and development of the Pacific and Iapetus margins of Gondwana during the Neoproterozoic and Paleozoic. Earth-Science Reviews 69, 249-279.

Clarke, D.B., 2019. The origins of strongly peraluminous granitoid rocks. The Canadian Mineralogist 57 (4), 529-550.

Coira, B., Cisterna, C.E., Ulbrich, H.H., Cordani, U.G., 2016. Extensional carboniferous magmatism at the western margin of Gondwana: las lozas valley, catamarca, Argentina. Andean Geology 43 (1), 105-146.

Collins, W.J., Beams, S.D., White, A.J.R., Chappell, B.W., 1982. Nature and origin of A-type granites with particular reference to south-eastern Australia. Contributions to Mineralogy and Petrology 80, 189-200.

Creaser, R.A., Price, R.C., Wormald, R.J., 1991. A-type granites revisited: assessment of a residual-source model. Geology 19, 163–166.

Dahlquist J.A., Morales Cámera M.M., Alasino P.H., Pankhurst R.J, Basei M.A.S., Rapela C. W., Moreno J.A. Baldo E.G, Galindo, C., 2021. A review of Devonian-Carboniferous magmatism in the central region of Argentina, pre-Andean margin of SW Gondwana. Earth-Science Reviews 221, 103781

Dahlquist, J.A., Alasino, P.H., Basei, M.A.S., Morales Cámera, M., Macchioli Grande, M., da Costa Campos Neto, M., 2018. Petrological, geochemical, isotopic, and geochronological constraints for the Late Devonian - Early Carboniferous magmatism in SW Gondwana (27–32° LS): an example of geodynamic switching. International Journal of Earth Sciences 107, 2575-2603.

Dahlquist, J.A., Alasino, P.H., Bello, C., 2014. Devonian F-rich peraluminous A-type magmatism in the protoAndean foreland (Sierras Pampeanas, Argentina): geochemical constraints and petrogenesis from the western-central region of the Achala batholiths. Mineralogy and Petrology 108, 391-417.

Dahlquist, J.A., Alasino, P.H., Eby, G.N., Galindo, C., Casquet, C., 2010. Fault controlled Carboniferous A-type magmatism in the proto-Andean foreland (Sierras Pampeanas, Argentina): geochemical constraints and petrogenesis. Lithos 115, 65-81.

Dahlquist, J.A., Pankhurst, R.J., Gaschnig, R.M., Rapela, C.W., Casquet, C., Alasino, P.H., Galindo, C., Baldo, E., 2013. Hf and Nd isotopes in Early Ordovician to Early Carboniferous granites as monitors of crustal growth in the Proto-Andean margin of Gondwana. Gondwana Research 23, 1617-1630.

Dall'Agnol, R., Frost, C.D., Ramo, T., 2012. IGCP Project 510 “A-type granites and related rocks through time”: project vita, results and contribution to granite research. Lithos 151, 1-16.

Dávila, F.M., Martina, F., Parra, M., Ávila, P., 2021. Effects of uplift on Carboniferous exhumation and mountain glaciations in pericratonic areas of SW Gondwana, central Argentina. Tectonics, 40, e2021TC006855.

De la Hoz, M., Coniglio, J., Kirschbaum, A., 2014. El Granito Los Ratones como posible fuente de flúor en la formación de sistemas epitermales, Sierra de Fiambalá, Catamarca. Serie Correlación Geológica 30(2), 77-91.

Debon, F., Le Fort, P. 1983. A Chemical-Mineralogical Classification of Common Plutonic Rocks and Associations. Transactions of the Royal Society of Edinburgh: Earth Sciences, 73, 135-149. http://dx.doi.org/10.1017/S0263593300010117

Debon, F., Le Fort, P. 1988. A cationic classification of common plutonic rocks and their magmatic associations: principles, method, applications. Bulletin de Minéralogie 111, 493-510.

Dora, M.L., Randive, K., Meshram, R., Meshram, T., Baswani, S.R., Korakoppa, M., Malviya, V.P., 2022. Petrogenesis of a calc-alkaline lamprophyre (minette) from Thanewasna, Western Bastar Craton, Central India: insights from mineral, bulk rock and in-situ trace element geochemistry. Geological Society, London, Special Publications, 513(1), 179-207.

Ernst, R.E., Buchan, K.L., 2003. Recognizing mantle plumes in the geological record.
Annual Review of Earth and Planetary Sciences 31, 469-523.

Eby, G.N., 1990. The A-type granitoids: a review of their occurrence and chemical characteristics and speculations on their petrogenesis. Lithos 26, 115-134.

Eby, G.N., 1992. Chemical subdivision of the A-type granitoids: petrogenetic and tectonic implications. Geology 20, 641-644.

Eby, G. N., 2011. A-type granites: magma sources and their contribution to the growth of the continental crust. Seventh Hutton Symposium on Granites and Related Rocks, p. 50-51.

Ezpeleta, M., Rustan, J.J., Balseiro, D., Davila, F.M., Dahlquist, J.A., Vaccari, N.E., Sterren, A.F., Prestianni, C., Cisterna, G.A., Basei, M, 2020. Glaciomarine sequence stratigraphy in the Mississippian Río Blanco Basin, Argentina, southwestern Gondwana. Basin analysis and palaeoclimatic implications for the Late Paleozoic Ice Age during the Tournaisian. J. Geol. Soc. Lond. 177, 1117-1128.

Faure, G., 1986. Principles of Isotope Geology, 466 pp, second ed. Wiley, New York.

Frost, B.R., Barnes, C.G., Collins,W.J., Arculus, R.J., Ellis, D.J., Frost, C.D., 2001. A geochemical classification for granitic rocks. Journal of Petrology 42, 2033-2048.

Frost, C.D., Frost, B.R., 2011. On ferroan (A-type) granites: their compositional variability and modes of origin. Journal of Petrology 52, 39-53.

González Bonorino, F., 1972. Descripción Geológica de la Hoja 13c, Fiambalá, Provincia de Catamarca. Subsecretaría de Minería de Buenos Aires.

Griffin, W.L., Belousova, E.A., Shee, S.R., Pearson, N.J., O'Reilly, S.Y., 2004. Archean crust evolution in the northern Yilgarn Craton: U-Pb and Hf-isotope evidence from detrital zircons. Precambrian Research 131, 231-282.

Grosse, P., Bellos, L.I., de los Hoyos, C.R., Larrovere, M.A., Rossi, J.N., Toselli, A.J., 2011. Across-arc variation of the Famatinian magmatic arc (NW Argentina) exemplified by I-, S- and transitional I/S-type Early Ordovician granitoids of the Sierra de Velasco. Journal of South American Earth Sciences 32, 110–126.

Höckenreiner, M., Söllner, F.,Miller, H., 2003. Dating the TIPA shear zone: an early Devonian terrane boundary between the Famatinian and Pampean systems (NW Argentina). Journal of South American Earth Sciences 16, 45-66.

Irvine, T.N., Baragar, W.R.A., 1971. A guide to the chemical classification of the common volcanic rocks. Canadian journal of earth sciences, 8(5), 523-548.

Ishikawa, K., Kanisawa, S., Aoki, K., 1980. Content and behavior of fluorine in Japanese Quaternary volcanic rocks and petrogenetic application. J Volc Geotherm Res 8, 161-175.

Jordan, T.E., Allmendinger, R.O., 1986. The Sierras Pampeanas of Argentina, a modern analogue to the Rocky Mountain Foreland deformation. American Journal of Earth Science 286, 737-768.

Larrovere, M.A, Casquet, C., Aciar, H., Baldo, E.G., Alasino, P.H, Rapela, C.W., 2021. Extending the Pampean orogen in western Argentina: new evidence of Cambrian magmatism and metamorphism within the Ordovician Famatinian belt revealed by new SHRIMP U-Pb ages. Journal of South American Earth Sciences 109, 103222.

Larrovere, M.A., Alasino, P.H., Baldo, E.G., 2016. La faja de cizalla dúctil doble vergente del noroeste de la sierra de Velasco: deformación de la corteza media durante la orogenia famatiniana. Revista de la Asociación Geológica Argentina 73 (1), 117-133.

Lazarte, J.E., 2013. Granitoides peraluminosos de mina San Antonio (tungsteno), Sierra de Vinquis norte, Sierras Pampeanas. Revista de la Asociación Geológica Argentina 70 (3), 427-435.

Li, X., Zhang, C., Wang, L., Behrens, H., Holtz, F., 2020b. Experiments on the Saturation of Fluorite in Magmatic Systems: Implications for Maximum F Concentration and Fluorine-Cation Bonding in Silicate Melt. Journal of Earth Science 31(3), 456-467.

London, D., 1997. Estimating abundances of volatile and other mobile components in evolved silicic melts through mineral-melt equilibria. Journal of Petrology 38, 1691-1706.

López de Luchi, M.G., Siegesmund, S., Wemmer, K., Nolte, N., 2017. Petrogenesis of the postcollisional middle devonian monzonitic to granitic magmatism of the Sierra de San Luis, Argentina. Lithos 288-289, 191-213.

Macchioli Grande, M., Alasino, P.H., Dahlquist, J.A., Morales Cámera, M.M., Galindo, C., Basei, M.A.S., 2020. Thermal maturation of a complete magmatic plumbing system at the Sierra de Velasco, Northwestern Argentina. Geological Magazine 158, 537-554.

Macchioli Grande, M., Alasino, P.H., Rocher, S., Larrovere, M.A., Uran, G.M., Reinoso, Carbonell, V., Moreno, G., 2019. Thermal evolution of upper crustal magmatic systems from the Sierra de Velasco, NW Argentina. Journal of Structural Geology 118, 1-20.

Mardonez, D., Julieta Suriano, J., Giambiagi, L., Mescua, J., Lossada, A., Creixell, C., Murillo, I., 2020. The Jachal river cross-section revisited (Andes of Argentina, 30◦S): constraints from the chronology and geometry of neogene synorogenic deposits. Journal of South American Earth Sciences 104, 102838.

Martin, R.F., 2006. A-type granites of crustal origin ultimately result from open-system fenitization-type reactions in an extensional environment. Lithos 91, 125-136.

Martin, R.F., 2012. The petrogenesis of anorogenic felsic magmas and AMCG suites: Insights on element mobility and mutual cryptic contamination from polythermal experiments. Lithos 151, 35-45.

Martina, F., Canelo, H.N., Dávila, F.M., Hollanda, M.E., Teixeira, W., 2018. Mississippian lamprophyre dykes in western Sierras Pampeanas, Argentina: evidence of transtensional tectonics along the SW margin of Gondwana. J. S. Am. Earth Sci. 83, 68-80.

Martina, F., Dávila, F.M., Hollanda, M.E., Teixeira, W., 2015. Edad y correlación de los lamprófiros paleozoicos del Famatina, Sierras Pampeanas de Argentina. XIV Congreso Geológico Chileno. Abstr. AT 1 Geología Regional y Geodinámica andina-101.

Martina, F., Viramonte, J.M., Astini, R.A., Pimentel, M.M., Dantas, E., 2011. Mississippian volcanism in the south-central Andes: new U-Pb SHRIMP zircon geochronology and whole-rock geochemistry. Gondwana Res. 19 (2), 524-534.

Middlemost, E.A., 1994. Naming materials in the magma/igneous rock system. Earth-Science Reviews 37 (3-4), 215-224.

Miller, C.F., McDowell, S.M., Mapes, R.W., 2003. Hot and cold granites? Implications of zircon saturation temperatures and preservation of inheritance. Geology 31, 529–532

Montero, P., Bea, F., Corretge, L.G., Floor, P.,Whitehouse, M.J., 2009. U-Pb ion microprobe dating and Sr-Nd isotope geology of the Galiñeiro Intrusive Complex. A model for the peraluminous/peralkaline duality of the Cambro-Ordovician magmatism of Iberia. Lithos 107, 227-238.

Morales Cámera, M.M., 2019. Estudio Petrológico, Geoquímico, Isotópico y Geocronológico de Granitos Peraluminosos Tipo A del Paleozoico Superior en Sierras Pampeanas: Batolitos de Achala y Vinquis. Tesis Doctoral (Ph.D.). Universidad Nacional de Córdoba, Argentina, p. 279 (unpublished). (In Spanish).

Morales Cámera, M.M., Dahlquist, J.A., Basei, M.A.S., Galindo, C., da Costa Campos Neto, M., Faccetti, N., 2017. F-rich strongly peraluminous A-type magmatism in the pre-Andean foreland Sierras Pampeanas, Argentina: Geochemical, geochronological, isotopic constraints and petrogenesis. Lithos 277, 210-227.

Morales Cámera, M.M., Dahlquist, J.A., García-Arias, M., Moreno, J.A., Galindo, C., Basei, M.A.S., Molina, J.F., 2020. Petrogenesis of the F-rich peraluminous A-type granites: an example from the devonian achala batholith (Characato Suite), Sierras Pampeanas, Argentina. Lithos 378-379, 105792.

Morales Cámera, M.M., Dahlquist, J.A., Ramacciotti, C.D., Galindo, C., Basei, M.A., Zandomeni, P.S., Grande, M.M., 2018. The strongly peraluminous A-type granites of the Characato suite (Achala batholith), Sierras Pampeanas, Argentina: Evidence of Devonian-Carboniferous crustal reworking. Journal of South American Earth Sciences 88, 551-567.

Moreno, J.A., Dahlquist, J.A., Morales Cámera, M.M., Alasino, P.H., Larrovere, M.A., Basei, M.A.S., Galindo, C., Zandomeni, P.S., Roche, S., 2020. Geochronology and geochemistry of the Tabaquito batholith (Frontal Cordillera, Argentina): geodynamic implications and temporal correlations in the SW Gondwana margin. Journal of the Geological Society 177, 455-474.

Moreno, J.A., Molina, J.F., Bea, F., Abu Anbar, M. & Montero, P. 2016. Th-REE- and Nb-Ta-accessory minerals in post-collisional Ediacaran felsic rocks from the Katerina Ring Complex (S. Sinai, Egypt): an assessment for the fractionation of Y/Nb, Th/Nb, La/Nb and Ce/Pb in highly evolved A-type granites. Lithos, 258-259, 173-196.

Moreno, J.A., Molina, J.F., Montero, P., Abu Anbar, M., Scarrow, J.H., Cambeses, A., Bea, F., 2014. Unraveling sources of A-typemagmas in juvenile continental crust: constraints from compositionally diverse Ediacaran post-collisional granitoids in the Katerina Ring Complex, southern Sinai, Egypt. Lithos 192-195, 56-85.

Muñoz, J.L., 1992. Calculation of HF and HCl fugacities from biotite compositions: revised equations. Geological Society of America, Abstracts with Programs 24, A221.

Nachit, H., Ibhi, A., & Ohoud, M. B., 2005. Discrimination between primary magmatic biotites, reequilibrated biotites and neoformed biotites. Comptes Rendus Geoscience, 337(16), 1415-1420.

Nelson, D.A., Cottle, J.M., 2018. The secular development of accretionary orogens: linking the Gondwana magmatic arc record of West Antarctica, Australia and South America. Gondwana Research 63, 15-33.

Paterson, S.R., Memeti, V., Mundil, R., Žák, J., 2016. Repeated, multiscale magmatic erosion
and recycling in an upper crustal pluton: implications for magma chamber dynamics and magma volume estimates, In: Special collection: perspectives on origins and evolution of crustal magmas. American Mineralogist 101, 2176-2198

Patiño Douce, A.E., 1995. Experimental generation of hybrid silicic melts by reaction of high-Al basalt with metamorphic rocks. Journal of Geophysical Research: Solid Earth, 100(B8), 15623-15639.

Patiño Douce, A.E., 1997. Generation of metaluminous A-type granitoids by low-pressure melting of calc-alkaline granitoids. Geology 25, 743-746.

Pearce, J.A., 2008. Geochemical fingerprinting of oceanic basalts with applications to
ophiolite classification and the search for Archean oceanic crust. Lithos 100, 14–48.

Pearce, J.A., Harris, N.B., Tindle, A.G., 1984. Trace element discrimination diagrams for the tectonic interpretation of granite rocks. Journal of. Petrology 25, 956-983.

Pilet, S., Baker, M.B., Stolper, E.M., 2008. Metasomatized lithosphere and the origin of alkaline lavas. Science, 320(5878), 916-919.

Ramos, V.A., Cristallini, E.O., Perez, D.J., 2002. The Pampean flat-slab of the Central Andes. Journal of South American Earth Sciences 15, 59-78.

Rapela, C.W., Pankhurst, R.J., Casquet, C., Dahlquist, J.A., Fanning, C.M., Baldo, E.G., Galindo, C., Alasino, P.H., Ramacciotti, C.D., Verdecchia, S.O., Murra, J.A., Basei, M.A.S., 2018. A review of the Ordovician Famatinian orogeny in southern South America: evidence of lithosphere reworking and continental subduction in the early proto-Andean margin of Gondwana. Earth-Science Reviews. 187, 259-285.

Rapela, C.W., Verdecchia, S.O., Casquet, C., Pankhurst, R.J., Baldo, E.G., Galindo, C., Murra, J.A., Dahlquist, J.A., Fanning, C.M., 2016. Identifying Laurentian and SW Gondwana sources in the Neoproterozoic to Early Paleozoic metasedimentary rocks of the Sierras Pampeanas: Paleogeographic and tectonic implications. Gondwana Research 32, 193-212.

Sallet, R., 2000. Fluorine as a tool in the petrogenesis of quartz-bearing magmatic associations: applications of an improved F-OH biotite-apatite thermometer grid. Lithos 50 (1), 241-253.

Sanematsu, K., Kon, Y., Gozalvez, R.M., Alvarez, D., Cecenarro, F., Iannizzotto, N.F., Yuki Tsunazawa, Y., Yokoyama, D.T., Herrmann, C., Zappettini, E.O., 2018. Geochemical Characteristics And U-Pb Zircon Ages Of Granites In A Tungsten- Mineralized District Of Catamarca Province In Sierras Pampeanas, Argentina. 15th Quadrennial IAGOD International Association on the Genesis of Ore Deposits Symposium, Salta, Argentina.

Siegel, C., Bryan, S.E., Allen, C.M., Gust, D.A., 2018. Use and abuse of zircon-based thermometers: a critical review and a recommended approach to identify antecrystic zircons. Earth-Science reviews 176, 87-116.

Sinclair, A.J. 1974. Selection of thresholds in geochemical data using probability graphs. Journal of Geochemical Exploration 3, 129-149.

Skjerlie, K.P., Johnston, A.D., 1992. Vapor-absent melting at 10 kbar of a biotite-bearing and amphibole-bearing tonalitic gneiss: implications for the generation of A-type granites. Geology 20, 263-266.

Skjerlie, K.P., Johnston, A.D., 1993. Fluid-absent melting behavior of an F-rich tonalitic gneiss at mid-crustal pressures: implications for the generation of anorogenic granites. Journal of Petrology 34, 785-815.

Söderlund, U., Patchett, J.P., Vervoort, J.D., Isachsen, C.E., 2004. The ^{176}Lu decay constant determined by Lu-Hf and U-Pb isotope systematics of Precambrian mafic intrusions. Earth and Planetary Science Letters 219, 311-324.

Sosic, M.V., 1972. Descripción Geológica de la Hoja 14d, Tinogasta, Provincias de Catamarca y La Rioja. Subsecretaría de Minería de Buenos Aires.

Stecher, O., 1998. Fluorine geochemistry in volcanic rock series: examples from Iceland and Jan Mayen. Geochimica et Cosmochimica Acta 62, 3117-3130.

Tischendorf, G., Förster, H.-J., Gottesmann, B. & Rieder, M. 2007. True and brittle micas: composition and solid-solution series. Mineralogical Magazine, 71, 285–320, https://doi.org/10.1180/minmag.2007.071.3.285

Toselli, G.A., Saavedra, J., Córdoba, G., Medina, M.E., 1992. Los granitos peraluminosos de las sierras de Vinquis, cerro Negro y Zapata (Sierras Pampeanas), provincia de Catamarca, Argentina. Estudios Geológicos 48, 247-256.

Vermeesch, P., 2018. IsoplotR: a free and open toolbox for geochronology. Geoscience Frontiers 9, 1479-1493.

Vervoort, J.D., Blichert-Toft, J., 1999. Evolution of the depleted mantle: Hf isotope evidence from juvenile rocks through time. Geochimica et Cosmochimica Acta 63, 533-556.

Villaseca, C., Barbero, L. and Herreros, V. 1998. A reexamination of the typology of peraluminous granite types in intracontinental orogenic belts. Transactions of the Royal Society of Edinburgh: Earth Sciences 89, 113-119.

Wang, G-C., Liu, Z., Tan, S-C., Wang, Y-K., He, X-H., Li, M-L., Qi, C-S., 2021. Petrogenesis of biotite granite with transitional I-A-type affinities: Implications for continental crust generation, Lithos 396-397, 106199.

Wang, L. X., Ma, C. Q., Zhang, C., Zhu Y-X, Marks, M.A.W., 2018. Halogen Geochemistry of I and A-Type Granites from Jiuhuashan Region (South China): Insights into the Elevated Fluorine in A-Type Granite. Chemical Geology 478, 164-182.

Whalen, J.B., Currie, K.L., Chappell, B.W., 1987. A-type granites: geochemical characteristics, discrimination and petrogenesis. Contributions to Mineralogy and Petrology 95, 407-419.

Whitney, D.L., Evans, B.W., 2010. Abbreviations for names of rock-forming minerals. American Mineralogist 95, 185-187.

Zandomeni P.S., Verdecchia S.O., Baldo E.G., Galindo C., Moreno J.A., Dahlquist J.A., Casquet C., Morales Cámera M.M., Basei M.A.S., Ramacciotti C.D., 2021. Early Ordovician magmatism in the Sierra de Ancaján, Sierras Pampeanas (Argentina): implications for the early evolution of the proto-Andean margin of Gondwana. Journal of Iberian Geology 47, 39-63.

Zappettini, E., Coira, B., Santos, J., Cisterna, C.E., Belousova, E., 2015. Combined U-Pb and Lu-Hf isotopes from the Las Lozas volcanics, Chaschuil Valley, NW Argentina: evidence of lower Pennsylvanian extensional volcanism in western Gondwana. Journal of South American Earth Sciences 59, 13-18.

Zen, E., 1986. Aluminum enrichment in silicate melts by fractional crystallization: some mineralogic and petrographic constraints. Journal of Petrology 27, 1095-1117.

FIGURE CAPTIONS

Fig. 1. Schematic geological map of west-central Argentina (Sierras Pampeanas) and the location of the studied region (Modified from Dahlquist et al., 2021). Abbreviations: ESP = Eastern Sierras Pampeanas, WSP = Western Sierras Pampeanas, Pc = Precordillera, FC = Frontal Cordillera, RPC = Río de la Plata craton. Granitic outcrops referred to in the text: SBIC = San Blas Intrusive Complex, HIC = Huaco Intrusive Complex, AB = Achala batholith. Mountain ranges: SL = San Luis, Co = Córdoba, LLR = Los Llano de La Rioja, VF = Valle Fértil, PP = Pie de Palo, SB = Sierra Brava, Ve = Velazco, An = Ancasti, Am = Ambato, AC = Aconquija, Ca = Capillitas, Be = Belén, Za = Zapata, Vi = Vinquis, Fi = Fiambalá, Fa = Famatina, TN = Toro Negro, Um = Umango.

Fig. 2. Geological map of the Sierra de Vinquis and the Sierra de Zapata with the location of the geological cross-sections and the geochemical samples of this and previous works.

Fig. 3. Rocks that compose the Andaluca Unit: (a) medium- to coarse-grained porphyritic biotite syenogranite from the northern sector of the AU, with a felsic enclave; (b) light orange coarse-grained porphyritic quartz monzonite from the central sector of the AU and (c) white coarse-grained porphyritic alkali feldspar granite containing pods formed by biotite and garnet from the southern sector of the AU. Dominant enclaves in the AU: (d) decameter-scale grey medium to coarse-grained porphyritic granitoid containing a higher amount of mafic minerals than the host. These enclaves are isolated but abundant and have ellipsoidal to irregular shape with a rounded outline. Enclave-host contacts are sharp and locally crossed by megacrysts. There are marginal schlieren and K-feldspar megacrysts accumulations in the rim of the enclaves; (e) scarce, isolated decimetre-scale aphanitic dark grey subvolcanic ovoid rock with scattered microcline phenocrysts and sharp enclave-host contacts locally crossed by megacrysts; (f) meter to decameter-scale light orange medium to coarse-grained porphyritic biotite monzogranite with abundant K-feldspar phenocrysts with angular to ovoid shapes and sharp, straight to irregular contacts. There are marginal schlieren and K-feldspar megacrysts accumulations of the host granite around the contact. Additionally, cm- to meter-wide irregular dykes of host-rock intrude this enclave; (g) Intrusive contact of the Andaluca syenogranite sharply cutting the magmatic foliation of the porphyritic biotitic monzogranite (Subunit E) of the VU. (h) Irregular dykes of the Andaluca porphyritic syenogranite intruded into an equigranular medium-grained biotite syenogranite.

Fig. 4. (a) SiO_2 vs. $Na_2O + K_2O$ wt.%, variation diagram (Middlemost, 1994) for the granitic samples from the Vinquis and Zapata intrusive complexes. The mid-alkaline/subalkaline magmatic lineages are defined by sigma isopleths (after Rittmann, 1957). The gray field represents Early Carboniferous metaluminous to weakly peraluminous A-type intrusive complexes (San Blas, Zapata and Fiambalá). Data from Dahlquist et al. (2010) and Morales Cámera et al. (2017). (b) P-Q diagram of granitoids under study (after Debon and Le Fort, 1983). Abbreviations: to = tonalite, gd = granodiorite, ad = adamellite, gr = granite, mzdq = quartz monzodiorite, mzq = quartz monzonite, qs = quartz syenite, mzgo = monzogabbro, mz = monzonite, s = syenite. (c) ASI (molar Al_2O_3 / [(CaO − 3.33 × P_2O_5) + Na_2O+K_2O]) vs. A/NK (molar Al_2O_3 / (Na_2O+K_2O)) diagram showing weakly and moderately to strongly peraluminous nature for the AU and VU, respectively. Boundary ASI = 1.1 from Chappell and White (1992). (d) A-B diagram (modified from Debon and Lefort, 1983; after Villaseca et al., 1998) showing dominant trends of ZIC, AU and VU. (e) FeO^t / (FeO^t + MgO) vs. SiO_2, wt.% diagram (Frost et al., 2001). The A-type granite field is after Frost et al. (2001). (f) $Na_2O + K_2O$ − CaO vs. SiO_2, wt.% diagram (Frost et al., 2001). (g) Bivariate diagrams for selected major and minor elements (concentrations are in wt. %) versus the TiO_2 (concentrations are in wt. %) of granitoids from the Sierra de Vinquis and Sierra de Zapata. Trend lines for AU (continuous) and VU (dotted).

Fig. 5. Chondrite-normalized (Boynton, 1984) REE plots for: (a) granitoids of the AU and (b) VU and ZIC. Primitive mantle-normalized (McDonough and Sun, 1995) spider diagrams for: (c) granitoids of the AU and (d) VU and ZIC. The gray and blue fields represent Early Carboniferous metaluminous to weakly peraluminous A-type intrusive complexes (San Blas, Zapata and Fiambalá) and VU, respectively. (e) Zr + Nb + Ce + Y vs ASI (molar Al_2O_3 / [(CaO − 3.33 × P_2O_5) + Na_2O+K_2O]) diagram showing the relationship between the peraluminosity of granitoids and their concentration in HFSE, where the metaluminous to weakly peraluminous granitoids of Andaluca and Zapata reach the typical concentrations of A-type granites (Zr + Nb + Ce + Y > 350 ppm after Whalen et al., 1987).

Fig.6. Bivariate diagrams for selected trace elements (concentrations in ppm) versus TiO_2 (concentrations in wt. %) of VIC and ZIC. Trend lines for AU (continuous) and VU (dotted).

Fig. 7. Plots of $\varepsilon Nd_{(t)}$ vs $^{87}Sr/^{86}Sr_{(t)}$. The stars show exponents of Early Carboniferous mafic igneous rocks related to A-type granitic magmatism of Sierras Pampeanas: Sample CG-175 (LLVS), alkaline basalt of the Las Lozas volcanic succession (Coira et al., 2016) and sample SBP-12 trachybasalt mafic dyke (Alasino et al., 2017). Data for Early Carboniferous metaluminous to weakly peraluminous A-type granites from Dahlquist et al. (2013). The composition of subcontinental lithospheric mantle (SCLM) for this region was estimated from the Ordovician gabbros and diorites outcropping in Sierras Pampeanas (data from Alasino et al., 2020). The compositions of enriched mantle reservoirs are from Ernst and Buchan (2003).

Fig. 8. U-Pb SHRIMP zircon dating of the samples (a) VIN-200 (quartz monzonite), (b) VIN-202 (garnet-bearing alkali feldspar granite) and (c) VIN-18 (two-mica monzogranite) in Tera-Wasserburg plot (lefts) and *weighted mean* diagram (right). Also, it shows the calculated concordia and mean ages from data points selected in green, respectively. Selected zircon images it is also shown. Furthermore, in (c) the dominant inherited zircon ages are plotted in blue with their respective concordia age.

Fig. 9. Age versus εHft values for zircon hosted in VIN-200 (quartz monzonite of the AU), VIN-202 (garnet-bearing alkali feldspar granite of the AU) and VIN-18 (two-mica alkali feldspar of the VU). Additionally, it is shown values for zircon hosted in VIN-1 (two-mica sienogranite of the VU; Morales Cámera et al., 2017), ZAP-33 (monzogranite of the ZIC; Dahlquist et al., 2013) and samples of A-type metaluminous to weakly peraluminous granitoids of Sierras Pampeanas (Dahlquist et al., 2013, Alasino et al., 2017).

Fig. 10. Composition of dark mica from the granitoids of the AU and ZIC. (a) Feal vs. mgli diagram (after Tischendorf et al., 2007). Abbreviations: Ann, annite; Cel, celadonite; Eas, eastonite; Hyp-mus, hyper-muscovite; Mus, muscovite; Mont, montdorite; Phl, phlogopite; Pol, polylithionite; Sid, siderophyllite; Tri, trilithionite. (b) MgO–FeO–Al_2O_3 discrimination diagrams (after Abdel-Rahman, 1994). (c) 10×TiO_2–FeO–MgO ternary diagram from Nachit et al. (2005).

Fig. 11. (a) F vs. $Fe^{2+}/(Fe^{2+}+Mg)$ diagram for biotites from this study and from Early Ordovician and Early Carboniferous calc-alkaline granites, and metaluminous and peraluminous A-type granites of Sierras Pampeanas. (b) Plot of atomic Mg/(Mg+Fe+Mn) vs. calculated F using the equations of Muñoz (1992). Estimated compositions for Carboniferous mafic magmatism are also projected (see Section 5.3). DPFC: Derraman Peralkaline Felsic Complex in the West African Craton (Morocco; Bea et al., 2016). KRC: Kaleriina Ring Complex (southern Sinai, Egypt; Moreno et al., 2014).

Fig. 12. (a) $^{87}Sr/^{86}Sr_{(350\ Ma)}$, (b) $\varepsilon Nd_{(350\ Ma)}$ and (c) $\varepsilon Hf_{(350\ Ma)}$ (zircon) of the studied AU, VU and ZIC. The thick gray bar represents the value range of the AU. Data of the ZIC are from Dahlquist et al. (2013) and VU from Morales Cámera et al. (2017). Boxplots of Pampean and Post-Pampean (meta-) sedimentary rocks (Sr, Nd) from the Rapela et al. (2018) and Morales Cámera et al. (2018) databases, (Hf in zircon) from Augustsson et al. (2016). Boxplots of Famatinian S-type and I-type granitoids (Sr, Nd) from the Rapela et al. (2018) database and (Hf in zircon) from Rapela et al. (2018) and Otamendi et al. (2017). The light blue circles correspond to the Peraluminous Ordovician granite Belen. Hf isotope data of the Carboniferous mafic rocks were calculated from the expression of Vervoort and Blichert-Toft (1999). The lower and upper caps at the end of each box indicate, respectively, the minimum and maximum values (outliers are not shown), the box limits are defined by the first and third quartiles, and the line in the center of the box represents the median.

Fig. 13. (a) Ce+Nb+Zr+Y vs. 10,000×Ga/Al granite discrimination diagram (Whalen et al., 1987). (b) Tectonic discriminant diagram (Pearce et al., 1984) for the studied granites. The Andaluca and Zapata granites plot in the within-plate granite field. (c) Studied granites plotted on the triangular Y–Nb–Ce diagram of Eby (1992) used to distinguish between different source rocks for A-type magmas. In these diagrams, the composition of the Carboniferous mafic magmatism (blue field) and the composition of the Carboniferous metaluminous to weakly peraluminous A-type magmatism (grey field) were projected (data from Alasino et al., 2012, Coira et al., 2016, Dahlquist et al., 2010).

Fig. 14. (a) alkaline vs SiO_2 diagram of the Carboniferous mafic magmatism associated with A-type granitic magmatism of NW Argentina (after Irvine and Baragar, 1971). (b) Th/Yb vs. Nb/Yb diagram showing as the mafic volcanic rocks plot dominantly in the MORB-OIB array, while the mafic dykes follow the arrows indicating the effects of magma-crust interaction (after Pearce, 2008) (Data from Alasino et al., 2012, 2017, Coira et al., 2016, Dahlquist et al., 2010).

Fig. 15. Conceptual model for the generation of the magmas of the VIC and ZIC in the retro-arc region showing the evolution of the multiple batches assembled incrementally into upper crust. See text for discussion. SP: strongly peraluminous; M-WP: metaluminous to weakly peraluminous.

Declaration of interests

☒ The authors declare that they have no known competing financial interests or personal relationships that could have appeared to influence the work reported in this paper.

☐The authors declare the following financial interests/personal relationships which may be considered as potential competing interests:

Table 1. Whole-rock compositions for the studied rocks from the Andaluca unit, Vinquis unit and Zapata Intrusive Complex. Major elements composition is recalculated to 100 wt.% volatile–free. Total iron as FeO_{tot}; Fe*= $FeO_{tot}/(FeO_{tot}+MgO)$. ASI= (molar Al_2O_3 / $[(CaO-3.33 \times P_2O_5)+Na_2O+K_2O]$). A/NK= (molar Al_2O_3 / (Na_2O+K_2O)). **TZr (°C) was calculated following to Watson and Harrison (1983).**

Reference		This work															
Latitude (S)		28.224141°	28.169194°	28.169464°	28.169464°	28.131499°	28.137075°	28.137075°	28.138380°	28,136052°	28.264487°	28.275216°	28.111263°	28.135653°	28.285016°	27.979778°	28.276492
Longitude (W)		67.350491°	67.317044°	67.333152°	67.333152°	67.321567°	67.312225°	67.31225°	67.312693°	67,315652°	67.407523°	67.39[illegible]99°	67.30[illegible]263°	67.316074°	67.373139°	67.225611°	67.378509°
Intrusive Complex		Vinquis															
Unit		Andaluca						Vinquis									
Clas		weakly peraluminous A-type									moderately to strongly peraluminous A-type						

Reference	Morales Cámera et al. (2017)									This work			Dahlquist et al. (2010)				
Latitude (S)	28.162111°	27.979139°	28.10[illegible]250°	28.110917°	28.[illegible]08250°	28.278889°	28.262194°	27.929461°	27.927481°	28.110091°	28.144916°	28.269126°	27°53′56″	27°53′39″	27°53′27″	27°53′17″	27°27′55″
Longitude (W)	67.240293°	67.231472°	67.229083°	67.220028°	67.229083°	67.338778°	67.289500°	67.251305°	67.242151°	67.326466°	67.416904°	67.413228°	67°22′22″	67°22′20″	67°21′27″	67°21′15″	67°16′34″
Intrusive Complex	Vinquis									Zapata							
Unit	Vinquis																
Clas	moderately to strongly peraluminous A-type									metaluminous to weakly							

ification																										peraluminous A-type							
Facies		Porphyritic alkali feldspar granite with Grt	Porphyritic quartz monzonite	Porphyritic quartz monzonite	Porphyritic biotite syenogranite	Porphyritic biotite syenogranite	Schlieren	Porphyritic biotite monzogranite (xenolith)	Equigranular biotite alkali feldspar granite	Equigranular biotite alkali feldspar granite	Porphyritic biotite monzogranite	Bt>Ms porphyritic monzogranite	Porphyritic biotite monzogranite	Porphyritic biotite monzogranite	Bt>Ms porphyritic monzogranite	Bt>Ms porphyritic monzogranite	Ms>Bt porphyritic syenogranite	Ms>Bt porphyritic syenogranite	Ms>Bt porphyritic syenogranite	Bt>Ms medium-grained equigranular monzogranite	Bt>Ms medium-grained equigranular monzogranite	Bt>Ms porphyritic monzogranite	Bt>Ms porphyritic monzogranite	Bt>Ms fine-grained equigranular monzogranite	Bt>Ms porphyritic monzogranite	Enclave	Bt-Amp porphyritic syenogranite	Porphyritic biotite syenogranite	Bt>Ms porphyritic alkali feldspar granite	Aplite	Porphyritic granite	Fine matrix porphyritic granite	Porphyritic granite	Fine matrix porphyritic granite
Samples		VIN-202	VIN-200	VIN-114	VIN-92	VIN-113	VIN-115	VIN-201	VIN-105	VIN-102	VIN-76	VIN-77	VIN-95	VIN-109	VIN-68	VIN-79	VIN-71	VIN-18	VIN-20	VIN-1	VIN-5	VIN-13	VIN-15	VIN-12	VIN-33	VIN-34	VIN-101	ZAP-204	VIN-73	ZAP-27	ZAP-29	ZAP-32	ZAP-33	ZAP-36

Elements	Detection limits																																
Major elements (wt. %)																																	
SiO_2	0.01	75.36	69.03	67.83	72.75	73.66	52.25	72.56	72.21	70.16	69.20	69.90	69.55	71.25	71.43	71.35	74.38	73.97	74.83	72.46	72.92	71.60	72.59	72.37	71.52	72.10	71.94	69.15	69.49	75.11	73.46	75.57	71.86	73.34
TiO_2	0.01	0.12	0.37	0.40	0.25	0.18	3.18	0.44	0.17	0.31	0.37	0.39	0.58	0.41	0.26	0.34	0.17	0.16	0.10	0.19	0.19	0.43	0.25	0.29	0.31	0.28	0.26	0.36	0.15	0.06	0.13	0.14	0.25	0.12
Al_2O_3	0.01	12.83	15.26	16.05	13.78	13.25	8.20	15.04	14.36	14.28	14.13	14.84	15.02	14.32	14.01	14.75	13.91	14.02	14.09	14.53	14.67	13.98	14.75	14.29	14.74	14.75	14.12	14.09	15.06	12.31	12.32	11.66	13.10	12.18
		1.	2.	2.	2.	1.	1	2.	1.	2.	2.	2.	3.	2.	1.	2.	1.	1.	0.	1.	1.	2.	1.	1.	2.	1.	2.	3.	0.	1	1.	1.	2.	1.

FeO_{tot}		57	29	47	20	95	8.41	59	76	74	46	47	15	38	74	04	31	29	76	31	31	36	56	87	20	89	17	04	97	.18	74	81	17	84
MnO	0.01	0.05	0.04	0.04	0.05	0.02	0.17	0.06	0.03	0.05	0.05	0.06	0.06	0.05	0.06	0.06	0.05	0.07	0.02	0.05	0.05	0.05	0.04	0.03	0.04	0.04	0.04	0.05	0.02	0.05	0.04	0.03	0.04	0.03
MgO	0.01	0.09	0.37	0.39	0.20	0.14	2.50	0.64	0.27	0.42	0.63	0.70	0.47	0.69	0.51	0.52	0.26	0.23	0.13	0.37	0.33	0.71	0.49	0.49	0.69	0.58	0.17	0.34	0.11	0.05	0.10	0.09	0.19	0.07
CaO	0.01	0.60	1.49	1.51	0.99	0.76	3.28	1.39	0.77	1.00	1.19	1.17	1.55	1.18	0.90	0.92	0.57	0.66	0.54	0.73	0.69	1.40	0.73	0.86	0.84	0.82	1.37	1.36	0.79	0.69	0.85	0.82	1.06	0.88
Na_2O	0.01	2.77	3.04	3.16	2.73	2.81	0.86	2.97	2.84	2.71	2.99	2.86	3.01	2.63	2.73	1.92	3.04	3.13	3.09	3.15	3.46	3.10	3.08	2.60	2.99	3.06	3.14	3.06	3.14	3.27	3.18	2.91	3.06	3.29
K_2O	0.01	5.77	6.81	7.02	6.03	6.47	3.48	6.19	6.81	7.23	5.34	5.30	5.43	5.51	5.00	5.42	5.01	4.76	5.26	5.03	4.85	4.55	5.42	5.82	5.15	5.13	5.91	6.25	6.78	5.43	5.18	5.03	5.70	4.98
P_2O_5	0.01	0.06	0.15	0.16	0.12	0.12	1.23	0.15	0.23	0.11	0.12	0.37	0.40	0.35	0.31	0.34	0.28	0.33	0.23	0.34	0.36	0.31	0.31	0.37	0.29	0.32	0.09	0.12	0.06	0.02	0.04	0.03	0.07	0.02
LOI		0.50	0.70	0.50	0.50	0.46	3.70	0.88	0.30	0.79	0.96	0.75	1.27	0.90	0.83	1.00	0.80	0.85	0.91	0.92	0.91	0.96	0.89	1.02	0.84	0.80	0.40	0.55	0.60	1.92	1.66	1.66	1.73	1.84
TOTAL		99.8	99.8	99.8	99.8	99.8	99.3	103.20	99.9	100.	97.71	99.28	100.84	99.94	97.97	99.89	99.9	99.4	99.9	99.08	99.73	99.46	100.07	100.01	99.62	99.7	99.8	98.7	97.2	100	98.88	99.9	99.4	98.7

		9	0	0	5	2	1		5	00							3	6	5							6	5	1	8	.23	9	5	7	9
Fe*		0.95	0.86	0.86	0.92	0.93	0.88	0.80	0.87	0.87	0.80	0.78	0.87	0.78	0.77	0.80	0.83	0.85	0.86	0.78	0.80	0.77	0.77	0.79	0.76	0.77	0.93	0.90	0.90	0.96	0.95	0.95	0.92	0.96
A/NK		1.19	1.23	1.25	1.25	1.14	1.58	1.30	1.19	1.16	1.32	1.39	1.39	1.39	1.41	1.38	1.33	1.36	1.31	1.37	1.34	1.30	1.35	1.35	1.40	1.39	1.22	1.19	1.20	1.09	1.14	1.14	1.17	1.13
A/CNK		1.08	1.01	1.03	1.07	1.02	0.74	1.07	1.07	1.01	1.10	1.16	1.10	1.15	1.21	1.19	1.21	1.22	1.20	1.22	1.20	1.11	1.20	1.18	1.22	1.22	1.00	0.99	1.08	0.98	0.99	0.99	1.00	0.98
ASI		1.09	1.04	1.06	1.10	1.03	1.00	1.09	1.11	1.04	1.12	1.25	1.18	1.23	1.30	1.28	1.29	1.31	1.26	1.30	1.29	1.18	1.28	1.27	1.30	1.31	1.02	1.01	1.09	0.99	1.00	1.00	1.01	0.99
AI		0.84	0.81	0.80	0.80	0.88	0.63	0.77	0.84	0.86	0.76	0.72	0.72	0.72	0.71	0.72	0.75	0.73	0.76	0.73	0.75	0.72	0.74	0.74	0.71	0.72	0.82	0.84	0.83	0.91	0.88	0.88	0.86	0.89
Trace elements (ppm)																																		
Cs	0.	5.7	6.8	7.6	4.7	7.7	21.	5.6	4.5	7.3	7.8	15.3	14.9	6.6	20.5	19.7	20.	27.	30.	20.6	13.6	5.9	17.1	6.9	15.4	18.	3.8	7.0	4.9	14	12.	14.	11.	12.

	1						3									2	6	3							1				.4	3	0	5	0
Rb	0.1	363.5	323.6	297.9	335.9	360.3	235.9	236.8	408.1	298.5	302.3	295.3	365.1	334.8	282.6	377.0	359.9	447.2	327.4	387.7	407.4	282.3	350.5	320.9	339.0	343.9	282.1	369.0	343.8	4229.0	5111.0	4700.0	3720.0	5560.0
Sr	0.5	24.5	120.1	147.5	69.5	14.9	82.0	116.9	50.4	21.7	97.8	79.1	89.5	74.8	55.4	59.6	34.3	26.8	29.2	45.8	36.9	116.[illegible]	[illegible].1	70.5	70.1	67.6	93.0	98.5	75.1	20.0	32.0	27.0	74.0	25.0
Ba	1	103	492	579	302	231	196	484	214	139	417	333	361	292	200	216	122	82	50	162	136	356	242	273	322	275	308	402	429	55	116	81	335	88
La	0.1	54.7	59.3	46.4	72.9	53.5	147.0	62.9	34.3	47.7	51.5	38.6	51.7	36.9	25.5	30.[illegible]	17.1	13.4	6.8	16.9	16.2	46.9	22.0	30.3	35.1	29.6	73.2	64.6	33.9	1111.0	59.6	89.0	53.4	99.8
Ce	0.1	123.8	117.6	91.8	164.5	103.1	382.1	131.7	79.8	108.[illegible]	121.9	85.[illegible]	115.3	87.0	57.6	72.8	36.0	29.9	15.3	37.8	36.5	103.1	48.6	68.2	74.7	64.7	157.4	140.8	76.2	2511.0	143.0	198.0	118.0	2310
Pr	0.02	14.62	13.50	10.61	18.90	14.48	49.99	14.87	9.45	[illegible].47	13.69	10.56	13.43	10.49	6.60	9.11	4.26	3.65	1.91	4.66	4.48	12.41	5.98	8.35	8.95	7.82	18.07	15.64	8.39	27.30	16.80	21.40	13.20	25.90
Nd	0.3	52.7	48.3	39.7	68.6	51.6	2109	50.8	34.2	49.3	47.6	36.2	48.3	41.0	23.9	34.2	16.6	13.5	7.1	17.3	16.7	46.6	22.3	30.9	32.8	29.0	64.2	53.6	27.8	92.3	64.5	71.5	46.3	891
Sm	0	1	8.	8.	1	1	4	8.	8.	1	11	8.	10	8.	5.	7.	3.	3.	1.	4.	4.	9.	5.	7.	7.	6.	1	1	6.	1	1	1	9.	1

	.05	2.89	98	36	4.25	0.20	8.73	94	50	0.07	.27	37	.08	81	68	33	69	43	79	37	12	39	13	44	31	96	3.06	1.99	69	7.10	5.10	4.30	71	9.50
Eu	0.02	0.44	1.53	1.71	0.99	0.52	1.01	1.43	0.66	0.48	1.23	0.98	1.14	0.91	0.65	0.72	0.42	0.38	0.28	0.50	0.44	1.13	0.63	0.74	0.87	0.78	1.63	1.62	0.85	0.82	0.50	0.42	1.01	0.48
Gd	0.05	12.86	8.00	8.48	13.20	9.13	48.76	6.27	8.13	9.24	9.48	7.10	8.28	6.80	5.05	5.64	3.46	3.19	1.63	3.77	3.44	6.74	4.05	6.14	5.59	5.39	11.18	10.51	5.54	13.60	13.90	11.30	8.65	16.20
Tb	0.01	2.54	1.27	1.27	2.25	1.34	6.99	0.85	1.49	1.48	1.55	1.09	1.15	1.00	0.79	0.79	0.57	0.63	0.31	0.64	0.60	0.97	0.62	1.02	0.80	0.84	1.69	1.66	0.90	2.34	2.77	2.13	1.79	3.24
Dy	0.05	16.36	6.65	7.13	14.17	7.92	41.75	4.97	9.52	8.89	9.69	5.86	6.97	5.57	4.79	4.27	3.70	3.77	1.91	3.36	2.92	5.00	3.21	5.42	3.93	4.06	10.37	9.63	5.40	12.50	17.00	12.50	10.60	20.00
Ho	0.02	3.73	1.38	1.31	2.69	1.45	7.28	0.91	1.67	1.87	1.04	1.35	0.87	0.82	0.68	0.61	0.68	0.36	0.52	0.47	0.90	0.55	0.92	0.63	0.64	1.82	2.07	1.15	2.31	3.33	2.39	1.99	3.86
Er	0.03	11.64	3.53	3.76	7.53	3.93	19.50	2.57	4.72	4.83	5.27	2.63	3.63	2.20	2.26	1.74	1.78	1.83	1.00	1.17	1.07	2.20	1.35	2.15	1.48	1.51	5.10	5.41	3.02	6.54	10.50	7.36	5.85	11.70
Tm	0.01	1.73	0.45	0.51	1.03	0.56	2.54	0.38	0.75	0.69	0.89	0.37	0.58	0.31	0.36	0.25	0.28	0.28	0.15	0.15	0.15	0.28	0.19	0.29	0.20	0.20	0.71	0.84	0.49	0.94	1.75	1.12	0.91	1.86

Yb	0.05	11.23	3.16	3.31	6.39	3.75	16.12	2.19	5.03	4.68	5.17	2.16	3.10	1.94	1.96	1.72	1.78	1.76	0.95	0.82	0.89	1.62	1.12	1.74	1.19	1.20	4.24	4.41	2.98	5.55	11.20	7.32	5.72	11.60
Lu	0.01	1.57	0.43	0.48	0.89	0.52	2.31	0.36	0.74	0.64	0.73	0.33	0.45	0.25	0.31	0.23	0.25	0.26	0.14	0.11	0.12	0.24	0.17	0.25	0.17	0.17	0.62	0.68	0.45	0.78	1.62	1.04	0.84	1.63
U	0.1	10.6	2.7	2.9	7.6	4.1	59.0	3.4	6.3	3.4	5.6	4.1	11.4	6.7	4.5	4.5	4.5	6.6	4.5	3.3	2.9	4.[illegible]	2.6	4.3	4.8	4.3	6.0	5.7	3.3	7.0	12.1	11.9	7.2	12.8
Th	0.2	44.1	28.3	24.4	55.6	36.7	55.1	31.2	30.7	36.7	41.1	27.7	37.0	30.9	18.1	27.2	11.2	9.6	6.1	11.[illegible]	11.0	31.8	14.1	20.7	19.7	17.5	54.7	47.0	27.8	57.8	53.0	70.1	28.4	78.6
Y	0.1	97.2	34.7	37.2	74.3	39.0	198.7	25.4	49.4	48.7	53.8	28.5	38.9	25.6	25.9	2[illegible].2	18.5	19.6	10.8	14.6	13.0	23.0	14.9	25.0	17.2	17.8	47.1	58.9	31.4	68.0	125.0	81.2	57.9	118.0
Nb	0.1	31.4	24.4	26.2	34.0	37.2	203.1	26.0	36.9	39.9	31.1	2[illegible].5	4[illegible].2	26.2	18.0	30.2	19.1	26.0	11.5	16.9	24.0	21.6	16.4	19.9	18.2	17.9	30.2	42.2	16.2	34.8	39.3	40.6	34.9	61.7
Zr	0.1	158.9	393.7	378.4	245.2	184.5	2728.3	227.7	148.3	2[illegible]9.6	184.5	163.2	240.6	169.4	98.3	161.7	90.4	70.6	37.2	86.7	81.0	180.6	105.1	145.5	141.0	132.1	340.7	328.4	1000.0	2644.0	1833.0	1920.0	2488.0	1888.0
Hf	0.1	5.4	10.5	10.1	7.9	6.1	70.8	6.4	4.9	6.8	5.8	4.8	7.5	5.3	3.2	4.6	2.8	2.4	1.5	2.8	2.6	5.1	3.1	4.3	4.2	4.0	9.8	9.2	3.3	8.3	6.3	6.9	6.9	7.4
Ta	0.1	1.6	1.5	1.6	1.6	1.4	11.0	2.2	1.7	2.1	2.4	2.3	5.3	2.4	2.8	3.0	2.4	4.0	2.2	3.5	3.4	2.5	2.1	1.6	2.1	2.6	1.7	3.4	1.6	2.9	5.9	5.5	4.3	9.0

Cr	1	<14	<14	<14	21	-	<14	3	<14	-	3	2	2	<14	2	<14	<14	6	5	7	6	7	9	7	12	10	<14	<1	<1	100	160	160	50	60
Sc	1	5	4	4	5	2	39	7	5	4	8	6	9	5	4	7	3	5	2	3	3	6	4	4	4	4	5	8	3	5	3	4	5	4
V	8	<8	14	19	13	9	129	27	13	21	25	25	44	33	16	27	18	12	9	15	13	36	26	20	29	24	9	<8	<8	8	6	6	8	<5
Ga	0.5	20.0	22.2	21.1	20.2	23.0	21.5	18.8	18.4	22.2	19.5	18.4	22.6	20.3	17.2	21.4	17.4	24.0	19.4	22.0	22.7	20.9	21.5	19.9	22.1	22.9	22.9	23.5	17.7	25.0	25.0	22.0	21.0	24.0
Pb	0.1	-	-	-	-	21.8	-	26.4	-	23.4	35.9	32.4	30.1	-	26.2	-	-	23.8	27.0	27.3	24.4	26.7	30.2	33.2	31.2	30.3	-	32.2	32.9	34.0	41.0	35.0	32.0	37.0
Ni	0.1	<20	<20	<20	<20	-	<20	2.8	<20	1.4	2.2	1.6	1.6	<20	1.5	<20	<20	2.3	0.8	4.2	3.1	4.4	4.7	3.0	3.5	2.4	<20	0.9	0.6					
Be	1	7	8	6	4	6	4	3	1	6	5	11	5	16	16	18	7	-	-	-	-	-	-	-	-	-	8	6	3	7	8	7	7	7
Co	0.2	28.3	24.6	2.6	1.8	12.8	23.7	37.4	1.4	12.3	23.5	23.0	50.5	4.1	26.4	3.0	1.3	-	-	-	-	-	-	-	-	-	1.6	32.3	21.3	2.0	1.0	1.0	2.0	<1
Sn	1	4	5	5	5	5	4	4	5	4	8	6	14	10	6	15	7	-	-	-	-	-	-	-	-	-	5	10	6	6	12	12	9	8
W	0.5	146.0	158.0	1.8	0.9	169.6	6.0	207.6	<0.5	107.4	134.6	146.1	333.4	0.7	154.4	8.1	6.5	-	-	-	-	-	-	-	-	-	<0.5	184.9	143.6	3.1	3.0	7.8	1.7	7.7
Cu	0.1	-	-	-	-	-	-	3.1	-	-	3.6	4.3	3.7	-	1.2	-	-	1.5	6.9	2.3	9.4	3.6	2.9	1.2	1.6	5.2	-	2.9	1.1	30.0	10.0	10.0	<10	<10
Zn	1	-	-	-	-	-	-	58	-	4	57	68	64	-	49	-	-	4	2	60	66	68	63	62	79	7	-	7	2	5	4	3	4	3

										0								7	9							3		0	4	0	0	0	0	0
$(La/Yb)_N$	-	3.3	12.5	9.5	7.7	9.7	6.2	19.3	4.6	6.9	6.7	11.8	11.2	13.1	8.6	12.1	6.4	5.0	4.6	14.2	12.1	19.8	13.5	12.0	19.9	16.6	11.8	9.9	7.6	13.5	3.6	8.2	6.3	5.8
$(Eu/Eu^*)_N$	-	0.09	0.54	0.62	0.22	0.16	0.06	0.57	0.26	0.15	0.35	0.40	0.37	0.36	0.40	0.33	0.34	0.37	0.54	0.37	0.33	0.42	0.47	0.32	0.42	0.39	0.40	0.44	0.45	0.16	0.11	0.10	0.34	0.08
Zr+Nb+Ce+Y		411	570	534	518	364	3512	411	314	427	391	298	435	308	200	285	164	146	75	156	194	328	185	259	251	232	575	570	224	618	490	512	459	599
10000*Ga/Al		2.9	2.7	2.5	2.7	3.3	4.6	2.4	2.4	2.9	2.5	2.3	2.8	2.6	2.2	2.7	2.3	3.0	2.5	2.9	2.9	2.7	2.9	2.6	2.8	2.9	3.0	3.1	2.1	3.8	3.7	3.5	3.0	3.6
TZr	-	793	860	856	828	798	987	817	781	811	802	795	824	80[illegible]	7[illegible]3	799	754	735	686	749	743	803	763	790	789	784	850	841	747	830	796	803	821	798

Table 2. Rb-Sr and Sm-Nd data for the studied rocks from Andaluca unit, Vinquis unit and Zapata Intrusive Complex.

Sample	Unit	Facies	t (Ma)	Sm (ppm)	Nd (ppm)	$^{147}Sm/^{144}Nd$	$^{143}Nd/^{144}Nd$	±StdErr*10^{-6}	$(^{143}Nd/^{144}Nd)_t$	εNd_t	$(^{143}Nd/^{144}Nd)_{350}$	εNd_{350}	Rb (ppm)	Sr (ppm)	$^{87}Rb/^{86}Sr$	$^{87}Sr/^{86}Sr$	±StdErr*10^{-6}	$(^{87}Sr/^{86}Sr)_t$	εSr_t	$(^{87}Sr/^{86}Sr)_{350}$	εSr_{350}	References
VIN-92	Andaluca	Porphyritic biotite syenogranite	342	14.25	68.60	0.1256	0.512292	2	0.512012	-3.65	0.512006	-3.58	335.9	89.50	14.0910	0.782563	3	0.713965	140.07	0.712356	117.35	This work
VIN-114	Andaluca	Porphyritic quartz monzonite	346	8.36	39.70	0.1273	0.512347	2	0.512060	-2.68	0.512047	-2.58	297.90	147.50	5.8627	0.738038	3	0.709162	71.93	0.708828	67.24	This work
VIN-115	Andaluca	Schlieren	346	48.73	210.90	0.1397	0.512358	1	0.512043	-2.95	0.512040	-2.92										This work
VIN-202	Andaluca	Porphyritic alkali feldspar granite with Grt	342	12.90	52.70	0.1480	0.512350	1	0.512020	-3.49	0.512013	-3.44	363.5	24.5	43.7972	0.910169	5	0.696955	-101.52	0.691955	-172.40	This work
VIN-109	Vinquis	Porphyritic biotite monz	359	8.81	41.00	0.1299	0.512158	2	0.511854	-6.31	0.511862	-6.38										This work

VIN-71	Vinquis	ogranite Ms>Bt porphyritic syenogranite	359	3.70	16.60	0.1348	0.512219	1	0.511904	-5.34	0.511912	-5.41	359.9	34.3	30.8641	0.873508	2	0.715767	165.95	0.719731	222.10	
VIN-79	Vinquis	Bt>Ms porphyritic monzogranite	359	7.3	34.2	0.1291	0.512165	1	0.511863	-6.13	0.511871	-6.21	[illegible]	59.6	18.5000	0.814600	3	0.720050	226.77	0.722426	260.37	
VIN-105	Vinquis	Equigranular biotite syenogranite Bt>Ms	359	8.5	34.2	0.1503	0.512271	2	0.511920	-5.03	0.511929	-5.09	408.1	50.4	23.7321	0.836394	3	0.715104	156.53	0.718152	199.67	
VIN-1	Vinquis	medium-grained equigranular monzogranite	359	4.37	17.33	0.1[illegible]2	0.512121	2	0.511764	-8.06	0.511773	-8.11	387.70	45.80	24.8250	0.842542	3	0.715665	164.50	0.718854	209.64	Morales Cámera et al. (2017)
VIN-15	Vinquis	Bt>Ms porphyritic monz	359	5.13	22.28	0.1391	0.512117	1	0.511792	-7.52	0.511800	-7.59	350.50	61.20	16.7459	0.812143	3	0.726558	319.21	0.728709	349.61	

		ogranite																				
VIN-18	Vinquis	Ms>Bt porphyritic syenogranite	359	3.43	13.46	0.1541	0.512224	1	0.511864	-6.13	0.511873	-6.18	447.20	26.80	49.4277	0.945857	3	0.693241	-153.99	0.699589	-63.97	
ZAP-26	Zapata Intrusive Complex	Porphyritic granite	340	17.1	92.3	0.1120	0.512258		0.512010	-3.74	0.512003	-3.63	43[illegible]	[illegible]31	24.1444	0.820759		0.703908	-2.80	0.700463	-51.57	
ZAP-27	Zapata Intrusive Complex	Aplite	340	18.6	69.6	0.1616	0.51243		0.512072	-2.54	0.51[illegible]062	-2.49	506.8	19.3	78.4742	1.038146		0.658356	-649.74	0.647158	-808.63	
ZAP-29	Zapata Intrusive Complex	Porphyritic granite	340	15.1	64.5	0.1416	0.512366		0.512[illegible]053	-2.91	0.512043	-2.84										Dahlquist et al. (2010)
ZAP-33	Zapata Intrusive Complex	Porphyritic granite	340	9.71	46.3	0.1268	0.51[illegible]306		0.512025	-3.45	0.512017	-3.36	378.9	73.1	15.1095	0.780833		0.707708	51.17	0.705552	20.71	
ZAP-35	Zapata Intrusive Complex	Porphyritic granite	340	6.6	33.8	0.1181	0.512297		0.512036	-3.24	0.512028	-3.14	313.7	44.1	20.7860	0.805605		0.705007	12.81	0.702041	-29.15	

t= crystallization age

Table 3. U-Pb SHRIMP for igneous zircon from samples VIN-200, VIN-202 and VIN-18.

							Total Ratios				Radiogenic Ratios*									Radiogenic				
Grain spot	U (ppm)	Th (ppm)	Th/U	$^{206}Pb_c$ (ppm)	$^{204}Pb/^{206}Pb$	f_{206} %	$^{238}U/^{206}Pb$	±	$^{207}Pb/^{206}Pb$	±	$^{238}U/^{206}Pb$	±	$^{207}Pb/^{206}Pb$	±	$^{207}Pb/^{235}U$	±	$^{206}Pb/^{238}U$	±	rho	$^{206}Pb/^{238}U$	±	$^{207}Pb/^{206}Pb$	±	% Disc
VIN-200																								
10.1**	159	93	0.58	7.3	0.00388	7.06	17.43	0.18	0.110	0.0131	18.76	0.27	0.05313	0.0160	0.391	0.1281	0.0533	0.0008	0.05	335	5	334	±685	-0
8.1**	199	110	0.55	9.1	0.00245	4.45	17.92	0.35	0.090	0.0074	18.75	0.39	0.05392	0.0095	0.396	0.0764	0.0533	0.0011	0.12	335	7	368	±397	+9
4.1**	89	70	0.78	4.2	0.00451	8.20	16.92	0.39	0.120	0.0110	18.43	0.50	0.05451	0.0168	0.408	0.1241	0.0543	0.0015	0.09	341	9	392	±680	+14
7.1	316	238	0.75	14.8	0.00162	2.95	17.87	0.17	0.077	0.0061	18.41	0.19	0.05311	0.0073	0.398	0.0545	0.0543	0.0006	0.08	341	3	334	±310	-2
6.1	464	266	0.57	21.9	0.00162	2.94	17.66	0.15	0.078	0.0045	18.40	0.17	0.05411	0.0056	0.410	0.0428	0.0550	0.0005	0.09	345	3	376	±234	+8
3.1	396	206	0.52	18.7	0.00096	1.75	17.87	0.15	0.068	0.0032	18.18	0.17	0.05438	0.0040	0.412	0.0309	0.0550	0.0005	0.12	345	3	387	±167	+11
9.1**	122	75	0.61	5.8	0.00327	5.95	17.06	0.18	0.104	0.0057	18.14	0.26	0.05603	0.0166	0.426	0.1262	0.0551	0.0008	0.05	346	5	453	±657	+24
11.1	281	176	0.63	13.4	0.00088	1.59	17.71	0.16	0.066	0.0032	18.00	0.17	0.05334	0.0041	0.409	0.0320	0.0556	0.0005	0.12	349	3	343	±176	-2
5.1	440	239	0.54	21.0	0.00115	2.09	17.61	0.19	0.077	0.0042	17.99	0.20	0.05422	0.0050	0.416	0.0388	0.0556	0.0006	0.12	349	4	380	±209	+8
2.1	364	187	0.51	18.0	0.00144	2.61	17.39	0.15	0.075	0.0055	17.34	0.17	0.05401	0.0066	0.429	0.0528	0.0577	0.0006	0.08	361	±4	371	±276	+3
1.1	123	85	0.69	6.6	0.00314	5.68	15.09	0.35	0.099	0.0084	16.00	0.40	0.05359	0.0114	0.462	0.0992	0.0625	0.0015	0.12	391	±9	354	±482	-11
VIN-202																								
1.1	139	118	0.85	6.6	0.00235	4.26	17.41	0.31	0.087	0.0087	18.18	0.35	0.05296	0.0112	0.402	0.0853	0.0550	0.0011	0.09	345	7	327	480	-6
2.1**	145	82	0.57	6.5	0.00362	6.59	17.85	0.18	0.106	0.0123	19.11	0.46	0.05283	0.0219	0.381	0.1582	0.0523	0.0013	0.06	329	8	322	941	-2
4.1	347	153	0.44	16.1	0.00131	2.39	18.06	0.15	0.073	0.0041	18.50	0.17	0.05391	0.0053	0.402	0.0398	0.0540	0.0005	0.09	339	3	367	222	+8
5.1	165	80	0.48	7.9	0.00140	2.53	17.38	0.30	0.075	0.0069	17.84	0.32	0.05467	0.0084	0.423	0.0657	0.0561	0.0010	0.12	352	6	399	346	+12
6.1**	547	311	0.5	24.7	0.000	1.3	18.	0.1	0.06	0.00	19.	0.1	0.052	0.00	0.38	0.02	0.05	0.00	0.1	331	3	315	13	-5

			7		73	3	75	5	3	22	01	6	69	30	2	20	26	04	5				0	
7.1**	394	215	0.55	17.3	0.00140	2.54	19.05	0.20	0.074	0.0039	19.54	0.22	0.05313	0.0050	0.375	0.0356	0.0512	0.0006	0.12	322	4	334	214	+4
8.1**	85	82	0.96	4.0	0.00439	7.98	16.78	0.39	0.117	0.0163	18.23	0.51	0.05275	0.0216	0.399	0.1635	0.0548	0.0015	0.07	344	9	318	929	-8
9.1	191	130	0.68	8.9	0.00255	4.64	17.65	0.16	0.092	0.0084	18.51	0.22	0.05441	0.0107	0.405	0.0801	0.0540	0.0006	0.06	339	4	388	443	+13
10.1	406	181	0.45	19.1	0.00215	3.92	17.55	0.15	0.085	0.0052	18.26	0.21	0.05315	0.0086	0.401	0.0651	0.0548	0.0006	0.07	344	4	335	367	-3
11.1	454	177	0.39	21.4	0.00090	1.64	17.91	0.20	0.067	0.0037	18.21	0.21	0.05426	0.0044	0.411	0.0349	0.0549	0.0006	0.14	345	4	382	182	+10
12.1	850	677	0.80	39.5	0.00047	0.85	18.33	0.16	0.061	0.0020	18.49	0.17	0.05450	0.0024	0.406	0.0258	0.0541	0.0005	0.20	340	3	392	99	+14
VIN-18																								
118-3.1**	300	164	0.54	14.4	0.00310	5.69	16.86	0.20	0.1004	0.0057	17.87	0.23	0.05499	0.0075	0.421	0.0579	0.0560	0.0007	0.09	351	4	396	307	+12
118-10.1	356	217	0.61	17.5	0.00290	5.20	16.57	0.15	0.0956	0.0022	17.49	0.18	0.05363	0.0045	0.423	0.0357	0.0572	0.0006	0.12	359	4	355	189	-1
118-8.1	615	122	0.20	30.7	0.00027	0.49	17.16	0.17	0.0587	0.0011	17.24	0.17	0.05473	0.0013	0.438	0.0112	0.0580	0.0006	0.38	363	3	401	53	+10
118-6.1	1033	95	0.09	52.2	0.00024	0.43	16.95	0.14	0.0574	0.0004	17.02	0.15	0.05393	0.0013	0.437	0.0112	0.0588	0.0005	0.33	368	3	368	54	+0
18-1.1a	780	228	0.29	38.2	0.00273	4.95	16.65	0.21	0.0939	0.0028	17.52	0.24	0.05405	0.0051	0.425	0.0408	0.0571	0.0008	0.14	358	5	373	214	+4
118-1.1	273	35	0.13	18.0	0.00061	1.09	12.58	0.12	0.0618	0.0019	12.72	0.12	0.05793	0.0026	0.628	0.0286	0.0786	0.0008	0.21	488	5	527	98	+8
118-4.1	554	44	0.08	38.0	0.00038	0.68	12.37	0.11	0.0624	0.0016	12.45	0.11	0.05686	0.0022	0.630	0.0245	0.0803	0.0007	0.23	498	4	486	84	-3
18-2.1	347	323	0.93	24.0	0.00174	3.11	12.04	0.11	0.0823	0.0071	12.43	0.11	0.05703	0.0102	0.633	0.1137	0.0805	0.0012	0.08	499	7	493	395	-1
18-1.1b	215	66	0.31	15.7	0.00224	4.00	11.31	0.12	0.0914	0.0085	11.78	0.14	0.05887	0.0100	0.689	0.1171	0.0849	0.0010	0.07	525	6	562	370	+7
18-4.1	275	26	0.09	18.4	0.00088	1.58	12.64	0.11	0.0700	0.0032	12.85	0.12	0.05719	0.0040	0.614	0.0431	0.0779	0.0007	0.13	483	4	499	153	+3

Error in Temora reference zircon calibration was 0.36% for the analytical session.

* Common Pb corrected using measured ^{204}Pb.

Errors are 1-sigma; $^{206}Pb_c$ and f_{206} % indicate the common and radiogenic portions, respectively.

** Not included in the crystallization calculation (see discussion int
he text).

Table 4. Hf isotope data for igneous dated zircon from VIN-200, VIN-202 and VIN-18.

Sample	Grain spot	$^{176}Hf/^{177}Hf$	± 2 σ	$^{176}Lu/^{177}Hf$	± 2 σ	ƐHf(t)	t (Ma)	ƐHf(350)	T_{DM}
VIN 200	3.1	0.2821	0.00002	0.001257	0.000006	-16.48	345	-16.37	2322
VIN 200	6.1	0.2822	0.00003	0.001043	0.000004	-12.89	345	-12.78	2099
VIN 200	7.1	0.28215	0.00003	0.00107	0.00002	-14.75	341	-14.56	2212
VIN 200	8.1	0.28219	0.00003	0.00114	0.00002	-13.48	335	-13.16	2128
VIN 200	9.1	0.28228	0.00002	0.000753	0.000008	-9.97	346	-9.88	1918
VIN 200	10.1	0.28235	0.00002	0.000542	0.000006	-7.68	335	-7.36	1736
VIN 200	11.1	0.28214	0.00001	0.00114	0.00002	-14.95	349	-14.93	2231
VIN 202	1.1	0.2824	0.0001	0.00106	0.00002	-5.82	345	-5.71	1657
VIN 202	2.1	0.28248	0.00005	0.00075	0.00009	-3.26	329	-2.81	1484
VIN 202	4.1	0.28238	0.00003	0.00063	0.00002	-6.55	339	-6.32	1699
VIN 202	5.1	0.28241	0.00002	0.00101	0.00008	-5.30	352	-5.34	1630
VIN 202	6.1	0.28233	0.00005	0.00083	0.00001	-8.54	331	-8.13	1817
VIN 202	7.1	0.2824	0.00002	0.000688	0.000005	-5.29	322	-5.62	1665
VIN 202	8.1	0.28236	0.00007	0.00108	0.00004	-7.26	344	-7.13	1747
VIN 202	9.1	0.2824	0.00001	0.000706	0.000004	-5.86	339	-5.63	1655
VIN 202	12.1	0.28233	0.00002	0.00081	0.00003	-8.35	340	-8.13	1812
VIN-18	118 3.1	0.28204	0.00003	0.00287	0.00007	-18.85	351	-18.87	2474
VIN-18	118 1.1	0.2815	0.0004	0.00349	0.00002	-35.40	488	-38.12	3596
VIN-18	118 4.1	0.28194	0.00004	0.00244	0.00005	-19.28	498	-22.31	2615
VIN-18	18 1.1a	0.2815	0.0001	0.0033	0.0002	-37.92	358	-38.08	3647
VIN-18	18 4.1	0.28143	0.00004	0.0041	0.0001	-38.18	483	-40.74	3760

t= crystallization age. T= model age. A two–stage continental model (T_{DM}) was calculated using the initial $^{176}Hf/^{177}Hf$ of zircon and the $^{176}Lu/^{177}Hf$ = 0.015 ratio for the lower continental crust (Griffin et al., 2004). Decay constant for ^{176}Lu of 1.867×10^{-11} y^{-1} was used (Soderlund et al., 2004). The present–day chondritic (CHUR) ratios of $^{176}Hf/^{177}Hf$ = 0.282772 and $^{176}Lu/^{177}Hf$ =

0.0332 from Blichert-Toft and Albarede (1997) were adopted to calculate εHf values. The present–day depleted mantle (DM) ratios of $^{176}Hf/^{177}Hf = 0.283225$ and $^{176}Lu/^{177}Hf = 0.038512$ from Vervoort and Blichert-Toft (1999) were adopted adopted to calculate T_{DM} values.

Highlights

The Andaluca plutonic unit of the Vinquis Intrusive Complex crystallized between 346 ± 3 Ma and 342 ± 3 Ma.

Andaluca Unit shows a F-rich weakly peraluminous ferroan A_2-type affinity.

The high contents of fluorine and HFSE in Andaluca Unit can be explained from an F-rich parental alkaline mafic magma.

The Andaluca Unit granitoids can be generated through combined crustal assimilation and fractional crystallization of magmas derived from the metasomatized subcontinental lithospheric mantle.